FLEXTAG: A Small and Self-renewable Protein Labeling System for Anti-fading Multi-color Super-resolution Imaging

Authors: Han Zhang[1], Yuan Yao[1,2,5], Xuye Wang[1], Yuan Tao[1,3], Haopeng Yang[1], Yinqi Wang[1], Mengde Liu[1,4], Marina Feric[1,2,3,5], Ruobo Zhou[1,2,3,4,*]

Affiliations: [1]Department of Chemistry, The Pennsylvania State University, University Park, PA 16802, USA
[2]Department of Biochemistry and Molecular Biology, The Pennsylvania State University, University Park, PA, 16802, USA
[3]The Huck Institutes of Life Sciences, The Pennsylvania State University, University Park, PA 16802, USA
[4]Department of Biomedical Engineering, The Pennsylvania State University, University Park, PA 16802, USA
[5]Center for Eukaryotic Gene Regulation, Penn State University, University Park, PA, 16802, USA

* To whom correspondence may be addressed. Email: ruobo.zhou@psu.edu

Abstract

Super-resolution fluorescence imaging enables visualization of subcellular structures and molecular interactions at the nanoscale, but its broader application has been hindered by long-standing limitations in current protein tagging systems, including rapid photobleaching, tag-induced artifacts, poor post-fixation labeling efficiency, and restricted multiplexing capability. Here, we present **FLEXTAG** (**F**luorescent **L**abeling for **E**xchangeable, **X**-resilient **T**agging in **A**dvanced **G**eneric Nanoscopy), a comprehensive protein labeling system comprising three orthogonal, ultrasmall (<20 kDa), and self-renewable protein tags that collectively overcome these major limitations of existing tagging systems, enabling optimized multi-color super-resolution imaging. Through continuous exchange of organic fluorophores, FLEXTAG supports unprecedented durations of high-resolution imaging in both live and fixed cells with minimal photobleaching. It is compatible with major super-resolution modalities, such as SIM, STED, STORM, and PAINT, and is applicable to a wide range of subcellar targets. To further address

fixation-induced labeling inefficiency and background fluorescence, we developed a novel protection-based fixation method and chemical blocking strategies that significantly preserve tag accessibility and enhance signal-to-noise ratio —improvements that are broadly applicable to other protein tagging systems. Altogether, FLEXTAG enables long-term tracking of dynamic behaviors and interactions of subcellular targets, as well as mapping of nanoscale protein organizations and cellular architecture, advancing both basic research and translational applications in cell biology.

Introduction

Fluorescence microscopy has revolutionized biological research by enabling the studies of cellular structures and dynamics across scales from single molecules to live animals, due to its unique advantages compared to other microscopies, such as high image contrast, high molecular specificity, non-invasive multi-color labeling capability, and long-term live imaging capability. Over the past decade, super-resolution fluorescence imaging, also known as fluorescence nanoscopy, has been invented to overcome the light diffraction limit and improved the spatial resolution from ~250 nm (this is ~50-fold larger than the average size of a protein) to molecular scale (1-20 nm)[1,2], allowing molecular-resolution fluorescence imaging. The most widely used nanoscopy techniques fall into two categories: 1) Patterned light illumination microscopy (PLIM), such as structured illumination microscopy (SIM) and stimulated emission depletion (STED) microscopy; 2) Single-molecule localization microscopy (SMLM), such as stochastic optical reconstruction microscopy (STORM)[3], photoactivated localization microscopy (PALM) [4], and point accumulation for imaging in nanoscale topography (PAINT)[5]. These advancements in spatial resolution enable the visualization of previously unresolvable subcellular details, such as

the organization of proteins within molecular complexes, nanoscale changes in cellular architecture, and dynamic molecular interactions, providing unprecedented mechanistic insights into biological processes.

The effectiveness of fluorescence nanoscopy relies on precise protein labeling strategies, which can be classified into three main approaches: 1) Immunofluorescence uses antibodies conjugated with organic dyes to recognize target proteins. While this method enables labeling of endogenous proteins, it is restricted to fixed-cell imaging. Additionally, only a small fraction of commercially available antibodies exhibit the high affinity and specificity required for nanoscopy, and their large size (~150 kDa) limits access to densely packed cellular structures; 2) Fluorescent protein tags, such as EGFP, mEos3.2[6], and mMaple3[7], allow live-cell imaging but are often outperformed in brightness and photostability by organic dyes; 3) Self-labeling protein tags, such as Halo-[8], CLIP- [9], and SNAP-Tag[10], provide site-specific labeling by reacting with small-molecule ligands conjugated to organic dyes. This approach offers improved photostability over fluorescent protein tags and is compatible with both live and fixed cells. However, even with organic dyes, photobleaching remains a major limitation, particularly in fluorescence nanoscopy, which requires prolonged high-intensity laser illumination. Additionally, in post-fixation labeling for fixed-cell imaging, commonly used fixatives such as paraformaldehyde (PFA) and glutaraldehyde (GA) can extensively crosslink proteins, reducing accessibility to dye-conjugated ligands and thereby lowering labeling efficiency of these self-labeling protein tags.

To mitigate photobleaching, self-renewable (i.e., exchangeable) protein tags have been recently developed, allowing continuous fluorescent dye replacement during imaging. Early efforts focused on fluorogenic GFP-like chromophores that reversibly bind to specific protein tags, such

as pFAST[11] and *blc* tags[12]. However, these chromophore-based renewable tags are incompatible with STED imaging due to their low brightness and photostability, and are also unsuitable for single-molecule localization microscopy (SMLM) such as STORM or PAINT: these chromophores lack the photoswitchability required for STORM, and under prolonged illumination in PAINT, they degrade into aldehyde derivatives that react with amines in the binding pocket[13], preventing chromophore rebinding (Supplementary Fig. 1a-1c). Additionally, these tags do not address the low post-fixation labeling efficiency caused by protein crosslinking during cell fixation. Another major challenge lies in expanding the spectral range of these tags for multi-color imaging, because chromophore binding is highly dependent on its precise chemical structure; even minor modifications to extend the color palette can disrupt tag recognition and reduce labeling efficiency. This limitation underscores the need to separate the fluorescent properties of the tag from its binding mechanism. More recently, HaloTag-based systems have been modified for reversible binding by engineering the HaloTag ligand to interact non-covalently[14]. This approach enables prolonged super-resolution imaging using both STED and PAINT. By linking nonfluorescent HaloTag ligands to various nanoscopy-compatible dyes, these systems (i.e., dye-conjugated HaloTag ligands) offer flexible color selection. However, the relatively large size of HaloTag (~33 kDa) can interfere with the native localization and function of tagged proteins, as evidenced by mislocalization when tagging ATP5ME, COX8, hYTHDC1, and the coronaviral envelope (E) protein[15] (Supplementary Fig.1d) and there are no similar self-renewable but orthogonal tags available that function across both PLIM- and SMLM-based techniques to enable three or more color super-resolution imaging. Furthermore, these existing tags do not overcome the challenge of low post-fixation labeling efficiency caused by protein crosslinking.

In this work, we present **F**luorescent **L**abeling for **E**xchangeable, **X**-resilient **T**agging in **A**dvanced **G**eneric Nanoscopy (**FLEXTAG**), a comprehensive framework that integrates three compact, self-renewable protein tags (FLEXTAG1, FLEXTAG2, and FLEXTAG3) with optimized labeling protocols to enable anti-fading multi-color super-resolution imaging. This FLEXTAG framework (Fig.1) distinguishes itself from previous protein tagging and labeling methods in the following six key aspects: 1) The tag sizes are small (<20 kDa) with minimal self-aggregation and tag-induced protein mislocalization issues, 2) The tags are self-renewable with minimal photobleaching, 3) It is compatible with both live and fixed cell imaging, 4) A protection-based fixation protocol has been developed to overcome low post-fixation labeling efficiency, 5) A chemical treatment and blocking protocol has been developed to minimize non-specific labeling, and 6) The tags are orthogonal and compatible with both PLIM-based and SMLM-based super-resolution imaging, providing a "one-for-all" solution, making it convenient to switch between different super-resolution imaging methods and enables three or more color super resolution nanoscopy. We envision this versatile super-resolution protein labeling system would allow for more flexible and detailed investigations on cellular processes, facilitating super-resolution imaging efforts to study molecular interactions, protein dynamics, and cellular functions.

Results

Development and characterization of FLEXTAG1

To develop new protein tags that address the limitations of current protein tagging systems, we sought to create a series of orthogonal, small, self-renewable protein tags (FLEXTAGs). These FLEXTAGs utilize synthetic fluorescent ligands, some of which are cell-permeable for live-cell

imaging, while others are designed specifically for fixed-cell applications. Upon entering the live cell or accessing fixed cellular structures, the fluorescent ligands reversibly bind to and dissociate from genetically encoded protein tags fused to target proteins, thereby minimizing photobleaching. To enable easy expansion for multi-color imaging, we decouple the fluorescent properties of the ligand from its binding to the tag by designing these fluorescent ligands with two components: a non-fluorescent part that specifically recognizes the protein tag and a nanoscopy-compatible dye, connected through a polyethylene glycol (PEG) linker. The criteria used for the tag development are: 1) minimal aggregation and small size (< 20 kDa) to minimize tag-induced mislocalization and potential malfunction of the tagged protein, 2) sufficiently high labeling efficiency for compatibility with all major fluorescence nanoscopic methods, and 3) dynamic exchange between the fluorescent ligand and protein tag to support PAINT imaging and effectively mitigate photobleaching across all major fluorescence nanoscopy techniques.

Based on these criteria, we developed FLEXTAG1 from a mutant form of the second bromodomain of human BRD4, $BRD4BD2^{L55A}$, a small protein degron tag (~15 kDa, about half the size of the commonly used EGFP tag). Originally designed for tag-targeted proteolysis, this tag can be specifically recognized by the small molecule ligand ET-JQ1[16]. JQ1 is a small molecule inhibitor of bromodomains that bind to wild-type BRD4BD2 ($BRD4BD2^{WT}$)[17]. To enhance binding specificity using the "bump-and-hole" strategy, an ethyl group was added to JQ1 to generate ET-JQ1 and the L55A mutation was introduced into BRD4BD2 to minimize off-target ligand binding to endogenous bromodomain proteins. Although this degron tag-ligand system has been successfully applied in tag-targeted proteolysis of human cells, it has not yet been further optimized for fluorescence imaging applications due to two challenges: 1) While ET-JQ1 shows minimal cross-reactivity with endogenous bromodomain proteins, as inferred

from western blot data where ET-JQ1 induces significantly less degradation of endogenous bromodomains than of BRD4BD2^{L55A}, this does not directly translate to imaging applications[16]. ET-JQ1 may still weakly and transiently bind to endogenous bromodomain proteins, generating unwanted fluorescence background; and 2) BRD4BD2 has a strong tendency to dimerize[18] meaning BRD4BD2^{L55A} could promote aggregation of the tagged protein, potentially altering its subcellular localization and function and leading to experimental artifacts.

To evaluate these two potential issues, we synthesized tetramethylrhodamine (TMR)-conjugated ET-JQ1 and JQ1 (as a control). After labeling U2OS cells, with and without overexpressing a bromodomain protein BRD4, using ET-JQ1-TMR and JQ1-TMR (Fig. 2a), we observed that ET-JQ1-TMR showed no detectable binding to either overexpressed BRD4-GFP or endogenous bromodomain proteins (Fig. 2c), whereas JQ1-TMR exhibited strong binding to overexpressed BRD4-GFP and detectable binding to the nucleus-localized endogenous bromodomain proteins, indicating that the ET-JQ1, in contrast to JQ1, has negligible binding affinity to endogenous bromodomain proteins under imaging conditions (Fig. 2b-2d). Next, we assessed the potential aggregation issue of BRD4BD2^{L55A}. Indeed, after labeling cells overexpressing BRD4BD2^{L55A}-tagged TOM20, a mitochondria-localized protein, with ET-JQ1-TMR, we observed severe aggregation of BRD4BD2^{L55A}, drastically altering the expected mitochondrial morphology and distribution (Fig. 2f).

To minimize the aggregation of BRD4BD2^{L55A}, we used ColabFold[19], an artificial intelligence system that predicts 3D structures of proteins and protein interactions from their amino acid sequences, to predict its dimer interface and identify the key interfacial interactions (≤ 3.5 Å bond distances), primarily between the Q115 residues of each monomer and between Y98 of one

monomer and M120 of the other (Fig. 2e**,** Supplementary Fig.2a). This predicted dimer interface closely resembles the intermolecular contacts observed in the crystal lattice formed by co-crystallizing BRD4BD1 and BRD4BD2[18], In addition, a previous study identified several mutations that reduce homodimer formation of BRD2BD1[20], a bromodomain that shares a nearly identical structure with BRD4BD2 (Supplementary Fig.2b). Based on the key interfacial residues identified from the predicted dimer interface and the previous mutations known to disrupt BRD2BD1 dimerization, we selected five mutations including Q21A, Y98K, Q115A, M120G, and F122E, to test their ability to disrupt BRD4BD2 dimerization while retaining ET-JQ1 binding. We introduced each of these mutations into the $BRD4BD2^{L55A}$ background and quantified the percentage of cells exhibiting abnormal (i.e., either bundled or aggregated) mitochondrial morphology when overexpressing TOM20 tagged with these BRD4BD2 variants (Hereafter referred to as the mitochondria morphology assay, which is a quantitative method for assessing the extent of protein tag aggregation; Supplementary Fig.3). Among the tested mutations, Q21A, Y98K, Q115A, and F122E failed to reduce $BRD4BD2^{L55A}$ dimerization. In contrast, M120G was the only mutation that effectively minimized dimerization-induced mitochondrial bundling or aggregation, reducing the percentage of cells with abnormal mitochondrial morphology from 80.0 ± 1.4% to 16.2 ± 3.4%, while still maintaining ET-JQ1 binding. Furthermore, M120G not only significantly reduced $BRD4BD2^{L55A}$ dimerization but also disrupted $BRD4BD2^{WT}$ dimerization, confirming the essential role of M120 in BRD4BD2 dimerization (Fig. 2g, Supplementary Fig.4).

As in our FLEXTAG system, we developed protection-based fixation method (described in a later section) to preserve tag accessibility after cell fixation and address low post-fixation labeling efficiency, where it requires adding a relatively high concentration (~ 100 μM) of the

ligand (ET-JQ1 for BRD4BD2$^{L55A,\ M120G}$ or JQ1 for BRD4BD2 ^{M120G}) during the cell fixation process to protect residues surrounding the binding pocket from fixation and hence prevent loss of ligand binding after fixation. Therefore, we performed additional tests to see if the tag remains prone to aggregation in the presence of its ligand ET-JQ1. Unfortunately, when incubating cells overexpressing TOM20 tagged with BRD4BD2^{L55A} or BRD4BD2$^{L55A,\ M120G}$ with 100 μM ET-JQ1, both constructs exhibited strong mitochondrial bundling and aggregation (Fig.2h, Supplementary Fig.4). The percentage of cells overexpressing BRD4BD2$^{L55A,\ M120G}$ with abnormal mitochondrial morphology increased from 16.2 ± 3.4 back to 100.0 ± 0.0%. Similarly, 100 μM JQ1-TMR increased the percentage of cells overexpressing BRD4BD2^{M120G} with abnormal mitochondrial morphology from 13.9 ± 1.9% to 32.1 ± 2.4%, although this ligand-induced aggregation was less pronounced than in BRD4BD2$^{L55A,\ M120G}$, indicating that ligand binding mediates a new dimer interface near the ligand binding pocket for both protein tags (Fig.2i, Supplementary Fig.4). To investigate this newly induced dimerization, we used ColabFold to predict the dimer of BRD4BD2$^{L55A,\ M120G}$. Although ColabFold does not support structure prediction of ligand-bound dimers, a new dimer interface, predicted in the absence of ligand, emerged near the ligand-binding pocket, with the key interfacial interactions between H105 residues of each monomer and between W42 of one monomer and A52 of the other (Supplementary Fig.2c). Based on the predicted new dimer interface, and that L55A exhibited more severe ligand-induced aggregation, we designed three variants to disrupt this new dimer interface: BRD4BD2$^{L55G,\ M120G}$, BRD4BD2$^{W42A,\ L55A,\ M120G}$, and BRD4BD2$^{L55A,\ H105A,\ M120G}$. Using the mitochondrial morphology assay (Supplementary Fig.3), we found that only BRD4BD2$^{L55A,\ H105A,\ M120G}$ disrupted the ligand-induced mitochondrial aggregation (Fig.2g, 2i, Supplementary Fig.4), while the other two mutants abolished ET-JQ1-TMR binding (Supplementary Fig.2d).

Next, following our criteria for FLEXTAG aforementioned, we evaluated the labeling efficiencies and the dynamic exchange rates between the fluorescent ligand and protein tag across several BRD4BD2 variants. To this end, we fused each BRD4BD2 variant, along with a fluorescent protein tag (mEGFP, used as an expression level reference for normalization), to the mitochondria-localized protein TOM20 (TOM20-mEGFP-BRD4BD2 variants). After labeling U2OS cells overexpressing a variant of TOM20-mEGFP- BRD4BD2 with JQ1-TMR (for variants without L55A mutation) or ET-JQ1-TMR (for variants with L55A mutation), we determined the fluorescence intensity ratios of TMR to mEGFP, which quantitatively represent the labeling efficiencies of each BRD4BD2 variant. Among the variants tested, BRD4BD2$^{L55A, H105A, M120G}$ exhibited the highest TMR/EGFP fluorescence ratio, indicating superior labeling efficiency (Fig.2j, Supplementary Fig.2d). Using PAINT imaging, we further quantified two dynamic exchange parameters in the presence of 1 nM ligand: 1) Event rate, defined as the average number of fluorescent ligand binding events per unit imaging area per unit time; 2) Apparent off- rate, defined as the average rate of disappearance of the single molecule fluorescent spot. While these rates do not precisely reflect the true ligand binding kinetics—since the apparent off-rate may be overestimated due to TMR photobleaching, and the event rate differs from the true on-rate as it is measured per imaging area rather than per tag—they still provide a practical assessment of PAINT compatibility. When these kinetic properties align with PAINT requirements, they often also help mitigate photobleaching in other nanoscopic techniques such as STORM, SIM, and STED. We found while the apparent off-rate of BRD4BD2$^{L55A, H105A, M120G}$ was slightly lower than other BRD4BD2 variants (Fig.2k), its event rate was significantly higher (Fig.2l), making it the most optimized for PAINT imaging.

Finally, we validated the performance of BRD4BD2$^{L55A,\ H105A,\ M120G}$ for tagging diverse proteins, localized to actin filaments, focal adhesions, the nucleus, vimentin, ER, and microtubules. The observed fluorescence patterns closely matched the expected localization and morphology of the targeted cellular structures (Fig.2m). We therefore designated BRD4BD2$^{L55A,\ H105A,\ M120G}$ as our developed FLEXTAG1.

Development and characterization of FLEXTAG2

We developed FLEXTAG2 from *E. coli* dihydrofolate reductase (eDHFR), a previously reported small (~18 kDa) protein imaging tag that can be specifically recognized by its specific small molecule inhibitor trimethoprim (TMP)[21] (Fig.3a). Although eDHFR and dye-conjugated TMP have been successfully used for protein imaging in live cells, this system remains largely incompatible with cell fixation, and its fluorescence signal is relatively weak due to low labeling efficiency[22,23] (defined as the percentage of protein tags in the fluorescent state at any given time). This inefficiency stems from the relatively low affinity of the non-covalent interaction between eDHFR and dye-conjugated TMP, leaving a large fraction of eDHFR tags in a dark, TMP-unbound state at any given time, limiting its applications in fluorescence nanoscopy where high fluorescence signal is often required. To address this, eDHFR mutations (e.g., L28C) and TMP variants have been developed to enable covalent bonding between eDHFR and TMP[22,23], However, this covalent interaction eliminates eDHFR's reversible binding and dissociation properties, which are crucial for mitigating photobleaching. Therefore, to achieve higher labeling efficiency while retaining its self-renewable nature of the tag, it is crucial to engineer eDHFR to enhance the binding rate constant (k_{on}) of TMP-dye binding to eDHFR.

Previous studies have reported that eDHFR has a relatively low thermal denaturation temperature T_m of 43°C[24], and exhibits low mechanical stability, with an average unfolding force of ~27 pN, much lower than that of most globular proteins[25]. These characteristics led us to hypothesize that its inherent instability partially contributes to insufficient labeling. This instability may result in a fraction of eDHFR molecules being in a conformational state in which TMP ligands cannot bind, thereby reducing fluorescence intensity. To test this hypothesis, we identified and designed ten eDHFR variants with potentially improved stability, categorized into four groups: 1) $eDHFR^{T68N, Q108D, T113V, E120P, S138Y}$ (eDHFR with quintuple mutations, termed $eDHFR^{QM}$), which has been reported to exhibit a higher T_m than wild-type eDHFR ($eDHFR^{WT}$)[26]; 2) $eDHFR^{P39C}$ and $eDHFR^{P39GCG}$. $eDHFR^{P39C}$, a mutant previously reported to have a higher midpoint denaturant concentration[27], features a Proline-39 to Cysteine (P39C) substitution, enabling disulfide bond formation between P39C and the cysteine-85 to stabilize the eDHFR structure. In $eDHFR^{P39GCG}$, P39 is substituted by GCG instead of C to allow additional flexibility for disulfide formation. 3) $eDHFR^{W22C, H149C}$ and $eDHFR^{W22GCG, H149GCG}$, where two residues in proximity, at positions 22 and 149, are substituted by either a C or GCG to enable disulfide bond formation between them; 4) $C(G)_n$-$eDHFR^{P89C}$,and $C(G)_5$-$eDHFR^{P89GCG}$ where n = 3, 5, 7. P89 is substituted by either C or GCG, and an additional amino acid sequence $C(G)_n$ is introduced at the N-terminus of eDHFR to promote disulfide bond formation between P89C and $C(G)_n$. Using ColabFold, we confirmed that all designed eDHFR variants, except for $eDHFR^{P39GCG}$, can form the intended disulfide bonds (Fig.3b, Supplementary Fig.5a-5d).

To compare the labeling efficiencies among the ten eDHFR variants, we utilized the similar double tagged TOM20 constructs (TOM20-mEGFP-eDHFR variants) as used for BRD4BD2 variants. After labeling U2OS cells overexpressing TOM20-mEGFP-eDHFR with TMR-

conjugated TMP (TMP-TMR) (Fig.3a), we determined the fluorescence intensity ratios of TMR to mEGFP, which quantitatively represents the labeling efficiencies of each eDHFR variant. The TMR/mEGFP fluorescence ratios for eDHFR$^{W22C,\ H149C}$ and eDHFR$^{W22GCG,\ H149GCG}$ dropped to nearly zero, indicating that mutations at positions 22 and 149 resulted in a near complete loss of TMP-TMR binding affinity. In contrast, all other eDHFR variants retained their TMP-TMR binding. Among these, eDHFR^{P39C} and eDHFR^{QM} showed a 30-40% increase in labeling efficiency, as indicated by the TMR/mEGFP ratio, compared to eDHFR^{WT}, while eDHFR^{P39GCG} exhibited labeling efficiency comparable to eDHFR^{WT}, consistent with ColabFold predictions indicating its inability to form a disulfide bond. Notably, C(G)$_n$-eDHFR^{P89C} variants exhibited greater labeling efficiency, with the highest enhancement (~3.3-fold) observed at the poly-glycine linker length of n = 5. Introducing additional glycine residues on both sides of cysteine (GCG) to increase flexibility decreased the labeling efficiency compared to a single cysteine mutation. Therefore, we selected C(G)$_5$-eDHFR^{P89C} for further optimization (Fig.3c, Supplementary Fig.5e).

Having identified that the length of poly-glycine linker between the N-terminal cysteine and the N-terminus of eDHFR^{P89C} affects labeling efficiency, we further aimed to optimize the linker length and sequence on the other side of the N-terminal cysteine (i.e., the linker between C(G)$_5$-eDHFR^{P89C} and the target protein). We designed the linkers of varying lengths (5, 10, and 20 amino acids) with different flexibilities, predicted using ColabFold (Fig.3d). By quantifying TMR/mEGFP ratios, we found that the 10 aa linkers yielded the highest labeling efficiency of C(G)$_5$-eDHFR^{P89C} compared to 5- or 20- amino-acid linkers. Among the tested sequences, the moderately flexible linkers resulted in the highest labeling efficiency compared to the flexible (i.e., GGGGS-based) or the rigid linkers (i.e., EAAAR-based) linkers. In contrast, the labeling

efficiency of eDHFR^{WT} was unaffected by linker length and flexibility, suggesting that the observed linker-dependent effect in C(G)$_5$-eDHFR^{P89C} is likely due to its influence on disulfide bond formation (Fig.3e, Supplementary Fig.6).

Next, we assessed the potential aggregation tendency of C(G)$_5$-eDHFR^{P89C}. Although eDHFR^{WT} is a monomer[28], we needed to confirm that C(G)$_5$-eDHFR^{P89C} mutation does not increase aggregation. Using the mitochondrial morphology assay, we found the percentage of cells overexpressing TOM20-mEGFP-eDHFR^{P89C} exhibiting aggregation was comparable to those overexpressing TOM20-mEGFP-eDHFR^{WT}. Additionally, the presence of 100 μM TMP, the concentration used in our protection-based fixation method, did not noticeably increase aggregation (Fig.3f, 3g, Supplementary Fig.7). To test whether the ligand binding kinetics of C(G)$_5$-eDHFR^{P89C} supports PAINT imaging, which also allows effectively mitigate photobleaching across all major fluorescence nanoscopic methods, we quantified event rate and apparent off- rate, as done for BRD4BD2 variants, at 1 nM TMP-TMR. C(G)$_5$-eDHFR^{P89C} exhibited the highest apparent on-rate (Fig.3h) and apparent off-rate (Fig.3i) in PAINT imaging, indicating that TMP binds to and dissociates from C(G)$_5$-eDHFR^{P89C} more rapidly than other eDHFR variants. This faster ligand exchange makes C(G)$_5$-eDHFR^{P89C} particularly well-suited for higher speed PAINT imaging. Indeed, PAINT images C(G)$_5$-eDHFR^{P89C} outperformed those obtained using eDHFR^{WT} (Fig.3j).

Finally, we evaluated the performance of C(G)$_5$-eDHFR^{P89C} for tagging proteins localized to diverse cell organelles, as done for FLEXTAG1. The obtained fluorescence images showed expected subcellular localization and morphology of the targeted cellular structures (Fig.3k). We therefore designated C(G)$_5$-eDHFR^{P89C} as FLEXTAG2.

Development and characterization of FLEXTAG3

We developed FLEXTAG3 from a mutant form of human FKBP, $FKBP^{F36V}$, a previously reported small (~12 kDa) protein tag used for tag-targeted proteolysis, chemical induction of protein interaction, and fluorescence imaging[29-31]. Based on the "bump-and-hole" strategy, the F36V mutation and its selective ligand SLF' (also known as AP1867) were developed to prevent undesired ligand binding to endogenous FKBPs. The high binding affinity of SLF' to $FKBP^{F36V}$ (K_D = 0.094 nM[30]) results in extremely slow exchange dynamics, making it incompatible with PAINT imaging and ineffective for mitigating photobleaching across major fluorescence nanoscopic methods. To enhance ligand exchange kinetics, a recent study identified the $FKBP^{F36L}$ mutant[32]. However, we found that overexpression of $FKBP^{F36L}$-tagged TOM20 in cells led to severe mitochondrial aggregation, with 74.3% ± 2.4% of cells exhibiting abnormal mitochondrial morphology (Fig.4e, 4f, Supplementary Fig.10), Structure prediction using ColabFold revealed that the $FKBP^{F36L}$ dimer interface is indeed mediated primarily through L36, with L36 of one monomer interacting with K34 and I90 of the other, along with additional interfacial contacts (Supplementary Fig.8a).

We next sought to identify mutations that could further disrupt the dimerization tendency of $FKBP^{F36V}$. ColabFold predictions showed a distinct dimer interface for $FKBP^{F36V}$ compared to $FKBP^{F36L}$, with interfacial interactions (bond distances ≤ 3.5 Å) observed between: 1) the side chain of T85 and the backbone of Q53, E54, and V55, 2) the side chains of F46 and P88, and 3) the side chains of Y82 and H87 (Supplementary Fig.8b). Unfortunately, this dimer interface lies near the ligand binding pocket. Despite multiple prediction rounds, we found that attempts to disrupt dimerization often resulted in structural disruptions to the binding pocket. Specifically,

introducing alanine substitutions or rationally designed mutations at all interfacial residues led to poor folding around the binding pocket, while failing to abolish dimer formation—new interfacial interactions formed, resulting in a similar overall dimer structure (Supplementary Fig.8c, 8e). To mitigate this, we narrowed our focus to only the strongest interfacial interactions (bond distances ≤ 3.0 Å), identifying E54–T85 and Y82–H87 as key interfacial contacts (Supplementary Fig.8d). We tested four mutations on the $FKBP^{F36V}$ background: E54A, H87A, H87D, and H87E. However, mitochondrial morphology assays showed that none significantly further reduce aggregation, with 17.2 ± 4.2%, 18.2 ± 3.5%, 35.3 ± 2.9%, and 18.2 ± 4.6% of cells displaying abnormal (i.e. aggregated or bundled) mitochondria, respectively (Fig.4f). The double mutant E54A/H87E also failed to further disrupt dimer formation, based on ColabFold predictions (Supplementary Fig.8e). Additionally, deletion of the Q53–V55 segment, intended to eliminate backbone-mediated interactions, resulted in severe protein misfolding (Supplementary Fig.8e). Therefore, despite extensive experimental and computational efforts, further reducing FKBP dimerization tendency remains a challenge. We therefore chose to proceed with $FKBP^{F36V}$, as it exhibits a tolerable aggregation profile, with ~20% of cells displaying mitochondrial bundling or aggregation.

To increase ligand binding kinetics to $FKBP^{F36V}$, we sought to evaluate alternative ligands and identify new mutations with the $FKBP^{F36V}$ scaffold. SLF'', a derivative of SLF' with the three methoxy groups removed, was reported to exhibit weaker affinity toward $FKBP^{F36V}$ than SLF'. To compare the labeling efficiencies of SLF' and SLF'', we labeled U2OS cells overexpressing double tagged TOM20 constructs (TOM20-mEGFP- $FKBP^{F36V}$) with TMR-conjugated SLF' (SLF'-TMR) and SLF'' (SLF''-TMR) (Fig.4b). Although SLF''-TMR exhibited reduced labeling efficiency to $FKBP^{F36V}$, considerable fluorescent signal in the cytosol of untransfected

cells suggested off-target binding of SLF''-TMR to endogenous FKBPs, making SLF' the preferred ligand for imaging applications (Fig.4c, 4d).

To further enhance SLF' binding kinetics while avoiding aggregation issues associated with $FKBP^{F36L}$, we engineered eight new single-point mutations near the SLF' binding pocket in $FKBP^{F36V}$ background: D37A, Q53A, E54A, V55A, I56A, H87A, I90A, and I91A. We assessed these variants for labeling efficiency using the TMR/mEGFP fluorescence ratios, and evaluated their event rates and apparent off rates using PAINT imaging (Fig.4a, Supplementary Fig.9a-9h).

Quantification of the TMR/mEGFP fluorescence ratio revealed that $FKBP^{F36V,\ D37A}$, $FKBP^{F36V,\ Q53A}$, and $FKBP^{F36V,\ H87A}$ exhibited higher brightness than $FKBP^{F36V}$, indicating increased affinity (i.e., lower K_D) (Fig.4h, Supplementary Fig.9i). However, PAINT imaging revealed that their higher affinity was largely due to prolonged binding (i.e., lower k_{off}), leading to the disappearance of localizations primarily due to photobleaching rather than dissociation. As a result, the apparent on- and off-rate calculations for these variants were inaccurate (as indicated by the asterisks in Fig.4i, 4j), implying that their exchange dynamics are insufficient to support PAINT imaging. For instance, in PAINT imaging, both $FKBP^{F36V}$ and $FKBP^{F36V,\ H87A}$ initially exhibited high single-molecule localization density benefit from their low K_D. However, the TMR fluorophores bound to the protein tag photobleached rapidly, and were not efficiently replenished by fresh SLF'-TMR. Consequently, localization density dropped sharply and maintained at a low level throughout the 45-minutes (30,000-frame) imaging duration (Fig.4k, 4l). Meanwhile, $FKBP^{F36A}$, $FKBP^{F36V,\ V55A}$, $FKBP^{F36V,\ I56A}$, $FKBP^{F36V,\ E54A}$, $FKBP^{F36V,\ I90A}$, and $FKBP^{F36V,\ I91A}$ exhibited lower brightness than $FKBP^{F36V}$, suggesting reduced affinity (i.e., higher K_D) (Fig.4h,

Supplementary Fig.9i). We found that FKBP$^{F36V, I91A}$ exhibited reasonable on- and off-rates for PAINT (slightly outperformed FKBP$^{F36V, E54A}$) (Fig.4i, 4j). As a result, the binding and dissociation of SLF'-TMR with FKBP$^{F36V, I91A}$ could continuously and stably generate localizations, making it well-suited for PAINT imaging (Fig.4k, 4l). Although optimizing exchange dynamics required some trade-off in affinity and fluorescence intensity during conventional imaging, the brightness of FKBP$^{F36V, I91A}$ remained sufficient to meet the demands of conventional fluorescence microscopy (Supplementary Fig.9i).

Finally, using the mitochondrial morphology assay, we found 19.0 ± 1.3% of TOM20-mEGFP-FKBP$^{F36V, I91A}$ expressing cells exhibited abnormal mitochondrial morphology (Fig.4e, 4f), similar to that observed for FKBP^{F36V}, and incubating these cells with 100 M SLF' did not further increase mitochondrial bundling or aggregation (Fig.4f, 4g, Supplementary Fig.10).

Finally, we validated the capability of FKBP$^{F36V, I91A}$ for tagging multiple organelles, as done for FLEXTAG1 and FLEXTAG2. The obtained fluorescence images showed expected subcellular localization and morphology of the targeted cellular structures (Fig.4m). Based on these results, we designated FKBP$^{F36V, I91A}$ as FLEXTAG3.

Development of post-fixation treatments to reduce non-specific binding for FLEXTAG

Although self-renewable protein tags offer many advantages over other fluorescence labeling methods and perform well for live-cell imaging as demonstrated by our three FLEXTAG tag/ligand systems, they face two major technical challenges in fixed-cell imaging: 1) Fixation with PFA or GA induces nonspecific binding of fluorescent ligands to biomolecule surfaces via hydrophobic and electrostatic interactions; and 2) Fixation partially hinders ligand access to the

tags, thereby reducing labeling efficiency by preventing a portion of the protein tags from binding to their ligands.

In immunofluorescence (IF), non-specific binding of primary or secondary antibodies to fixed cells is a common source of unwanted background fluorescence. To mitigate this, various strategies have been developed, including the use of alternative fixatives, and post-fixation treatments with specific reagents. Inspired by these strategies, we investigated whether similar strategies could reduce the non-specific binding of small-molecule fluorescent ligands, which are likely to interact with fixed biomolecules via similar hydrophobic and electrostatic mechanisms.

First, using TMP-TMR as a model fluorescent ligand, we sought to identify the optimal fixative that minimizes background fluorescence without compromising cellular structural integrity. To this end, we evaluated both the non-specific fluorescence background caused by TMP-TMR binding to fixed cells and the preservation of organelle morphology across four previously used fixatives: 1) 4.0% PFA; 2) 4.0% PFA + 0.1% GA; 3) 3.0% glyoxal[33]; and 4) 4.0% methacrolein[34]. For each fixative, we also examined the effect of post-fixation treatment with reducing agents, either NH_4Cl, or $NaBH_4$, which reduce non-specific binding by reacting with the excess aldehydes on fixed protein surface (Fig.5a). Without reducing agent treatment, the levels of non-specific binding followed the order: Glyoxal < PFA < PFA + GA ≈ methacrolein. Both reducing agents significantly reduced non-specific binding, with $NaBH_4$ yielding a much stronger reduction than NH_4Cl. After $NaBH_4$ treatment, the order of non-specific binding levels changed to: Glyoxal < PFA ≈ PFA + GA < methacrolein (Fig.5b, 5c). To assess structural preservation, we used IF to examine nuclear, mitochondrial, ER, and microtubule morphology following fixation. The extent of organelle morphology preservation followed the order:

methacrolein < Glyoxal < PFA < PFA + GA (Supplementary Fig.11). Based on these results, we recommend PFA + GA as the preferred fixative for FLEXTAG applications when minimizing fixation artifact is a priority, while glyoxal or PFA alone may further reduce nonspecific binding, albeit at the cost of reduced structural preservation.

To further eliminate non-specific binding, we evaluated the effectiveness of various blocking agents that may alter the microenvironment of fixed protein surfaces and reduce nonspecific interactions with ligands or dyes (Fig.5d). These include: 1) bovine serum albumin (BSA) and 2) Tween-20, both commonly used in IF to reduce antibody non-specific binding; 3) salmon sperm DNA, used in fixed cell RNA imaging to reduce non-specific binding of nucleic acid probes. 4) potassium thiocyanate (KSCN), a chaotropic salt previously reported to disrupt hydrophobic interactions in PAINT imaging[35] . Our results showed that BSA, Tween-20, and KSCN effectively decreased non-specific binding, whereas salmon sperm DNA had minimal impact. The combination of Tween-20, BSA, KSCN provided the most pronounced reduction in both conventional (Fig.5e, Supplementary Fig.12a) and PAINT imaging (Fig.5f), suggesting the nonspecific binding of fluorescent ligands is primarily mediated by hydrophobic interactions. Since KSCN has previously been reported to reduce the binding of phalloidin to F-actin, we evaluated its potential impact on ligand binding to the three FLEXTAGs. Quantification of fluorescence intensities from TMR-conjugated FLEXTAG ligands bound to FLEXTAG-tagged TOM20 showed no significant signal reduction after KSCN treatment, indicating that KSCN does not significantly affect ligand binding or labeling efficiency (Supplementary Fig.12b, 12c). To further investigate the role of hydrophobicity in non-specific ligand binding, we conjugated TMP to six dyes emitting in cyan-green range with varying hydrophobicity (measured by LogD): Cy2, BODIPY1, BODIPY2, rhodamine 110 (Rh110), fluorescein, and AF488 (Supplementary

Fig.13a). Quantification of their non-specific bindings in fixed cells revealed a positive correlation between non-specific binding and LogD values (Supplementary Fig.13b, 13c), consistent with prior observations[36]. These results suggest that selecting dyes with lower LogD values can help minimize non-specific interactions in fixed-cell imaging using FLEXTAG.

We next examined whether dye fluorogenicity could reduce background fluorescence arising either from non-specific binding to fixed cells or from freely diffusing fluorescent ligands during imaging. Rhodamines, a well-known fluorogenic dye family, undergo a conformational shift from a non-fluorescent lactone (closed) form to a fluorescent zwitterionic (open) form upon target binding. This property can suppress background fluorescence by minimizing signal from both non-specific binding and unbound ligands in the imaging buffer. We conjugated TMP to five rhodamines emitting in yellow-red range with various fluorogenicity ranging from non-fluorogenic ATTO565 and AF594 to the highly fluorogenic JF585[37,38] (Supplementary Fig.13a). Quantification of the two types of background fluorescnece signals revealed a negative correlation with fluorogenicity, indicating that more fluorogenic dyes produce less background fluorescence. These results suggest that fluorogenicity is another important factor to consider when selecting fluorophores for fixed-cell imaging using FLEXTAG (Supplementary Fig.13d-13f).

Development of protective fixation to preserve post-fixation labeling efficiency of FLEXTAGs

Fixation reduces the labeling efficiency of self-renewable protein tags through two main mechanisms: 1) aldehyde-based protein crosslinking and Schiff base formation can occur near or within the ligand-binding pocket, potentially limiting or obstructing ligand access; and 2)

crosslinking can restrict the protein tag's ability to undergo ligand-binding-induced conformational adaptation (i.e., ligand-induced fit), which stabilizes ligand binding. We hypothesized that preincubating live cells expressing FLEXTAG-tagged proteins with a high concentration of dye-free (unconjugated) FLEXTAG ligands as a protective reagent, followed by fixation in the presence of these unconjugated ligands, would protect the binding pocket by excluding aldehydes and simultaneously lock the protein into its ligand-bound conformation. This strategy, which we term "protective fixation" is designed to preserve the protein tags in a ligand-bindable state. After protective fixation, the unconjugated ligands are removed, and dye-conjugated ligands are subsequently applied for fixed-cell imaging (Fig.5g).

To evaluate the effectiveness of protective fixation and determine the optimal fixation conditions, we fixed U2OS cells stably expressing TOM20-mEGFP-FLEXTAG2 at room temperature (RT) using a fixation buffer containing 4.0% PFA + 0.1% GA, in the presence of varying concentrations (0–100 μM) of TMP. Cells were then labeled with 20 nM TMP-TMR. Labeling efficiency increased with TMP concentration and plateaued at 1 μM, confirming TMP's protective effect. Replacing TMP with methotrexate (MTX) (Fig.5h), a dihydrofolate reductase inhibitor [39] that exhibits ~60-fold higher affinity (K_i = 21 pM) for eDHFR compared to TMP (K_i = 1.3 nM)[40], did not further enhance labeling efficiency preservation, likely due to inefficient cellular uptake of MTX (Fig.5i, Supplementary Fig.14). Performing protective fixation at 37°C resulted in poorer labeling efficiency preservation compared to RT, likely due to increased ligand exchange dynamics at higher temperatures that prolonged the duration FLEXTAG2 remained unliganded during fixation (Fig.5j, Supplementary Fig.14). Fixation using PFA alone yielded similar trends but resulted in slightly lower labeling preservation compared to PFA + GA (Fig.5i, 5j, Supplementary Fig.14).

To quantify the preservation rate and evaluate general applicability across tags, we compared labeling efficiencies in live cells, fixed cells with protective fixation, and fixed cells without protective fixation for our three self-renewable tags as well as GFP-like chromophore-based renewable protein tag pFAST[11]. Protective fixation significantly improved labeling efficiency across all tags when using their corresponding protective agents during fixation: ET-JQ1, TMP, SLF', or HMBR (Fig.5h). Compared to live cells, labeling efficiency was preserved at 65.2 ± 7.5% for FLEXTAG1, 66.8 ± 2.7% for FLEXTAG2, 60.5 ± 1.9% for FLEXTAG3, and 49.7 ± 3.3% for pFAST, representing 4.5-, 8.8-, 3.9-, and 3.1-fold increases over fixation without a protective agent, respectively (Fig.5k, 5l). These results demonstrate that protective fixation is broadly effective at enhancing post-fixation labeling efficiency for self-renewable tags.

Lastly, we evaluated the cytotoxicity of the protective agents by assessing cell survival and mitochondrial/nuclear morphology following a 24-hour incubation at 37 °C with 100 μM HMBR, JQ1, ET-JQ1, TMP, MTX, or SLF'. While JQ1 caused acute cytotoxicity within 1–5 hours, the other agents exhibited only mild toxicity after 12 hours. Notably, the ligands used in the FLEXTAG system showed lower toxicity than HMBR, supporting their suitability for protective fixation (Supplementary Fig.15).

FLEXTAG enables PLIM-based nanoscopic imaging with anti-fade performance

After establishing the FLEXTAG framework including three small self-renewable protein tags, methods for reducing non-specific binding, and a labeling efficiency preservation strategy (i.e, protective fixation), we evaluated its performance in enabling anti-fade multi-color fluorescence nanoscopic imaging. Fluorescence nanoscopy methods fall into two main categories: 1) PLIM uses structured or patterned illumination to improve spatial resolution; and 2) SMLM relies on

the precise localization of single fluorophores that stochastically blink on and off, enabling the reconstruction of super-resolved images with nanometer precision.

We first assessed FLEXTAG in SIM, a fast PLIM-based nanoscopy offering ~100 nm spatial resolution. Unlike the pFAST ligand, which is a fluorescent chromophore, FLEXTAGs' ligand-binding components are non-fluorescent, allowing greater flexibility in spectral selection for multi-color imaging. To demonstrate this versatility, we synthesized FLEXTAG ligands conjugated to five dyes spanning distinct spectral ranges: four cell-permeable dyes (JF525, TMR, MaP555, and JF635) suitable for both live and fixed-cell imaging[37,38,41] and one cell-impermeable dye (AF594) for fixed-cell imaging only (Fig.6a). These enabled three-color live-cell co-staining of cells co-expressing TOM20-FLEXTAG1, MAP7-FLEXTAG2, and FLEXTAG3-Sec61β, targeting mitochondria, microtubules, and the ER, respectively. FLEXTAG-SIM imaging enabled us to directly visualize the spatial interactions among these organelles (Fig.6b). We further evaluated FLEXTAGs' performance in fixed cells using our protective fixation and nonspecific binding reduction protocols. SIM images from fixed cells closely resembled those from live cells, validating the applicability of FLEXTAG to fixed-cell imaging. (Fig.6d).

To assess the orthogonality of our three FLEXTAGs, we quantified the three-color SIM images and observed minimal crosstalk between color channels (Fig.6c), demonstrating the high orthogonality of our three protein tags for multiplexed imaging.

Next, we assessed FLEXTAG in STED, a PLIM-based nanoscopy offering higher spatial resolution than SIM by incorporating a depletion laser beam. FLEXTAG enabled two-color STED imaging in fixed cells co-expressing TOM20-FLEXTAG1 and Lifeact-FLEXTAG2 (or TOM20-FLEXTAG2 and Lifeact-FLEXTAG3), showing the expected mitochondrial and actin

cytoskeleton localizations, respectively, along with potential interactions between mitochondria and actin stress fibers (Fig.6e). Notably, our two-color FLEXTAG-STED imaging was performed on a STEDYCON system equipped with a single depletion laser, which limits emission depletion to two color channels. We anticipate that three-color STED imaging would be feasible with a STED microscope featuring multiple depletion lasers covering a broader wavelength range.

Photobleaching remains a major limitation for PLIM-based nanoscopy: SIM requires acquisition of tens of images to reconstruct a single SIM image; STED's high-power depletion lasers exacerbate fluorophore bleaching. FLEXTAG addresses this by dynamically replacing photobleached ligands with fresh fluorescent ones, maintaining relatively stable signals over time (Fig.6f). To quantify this anti-fade performance, we acquired time-lapse SIM images of TOM20 tagged with FLEXTAG1, FLEXTAG2, FLEXTAG3, HaloTag (a non- renewable protein tag), or $FKBP^{F36V}$ (the protein tag described above with slow renewable rate), each labeled with MaP555-conjugated ligands. Over 30 consecutive frames, fluorescence intensity dropped to 20% for HaloTag and 50% for $FKBP^{F36V}$. In contrast, the fluorescence intensity of all three FLEXTAGs remained nearly constant (Fig.6g, 6h). Repeating the experiment with JF635-conjugated ligands yielded similar results (Supplementary Fig.16). These findings highlight FLEXTAG's rapid self-renewal kinetics and its ability to overcome photobleaching during PLIM-based nanoscopic imaging.

FLEXTAG enables SMLM-based nanoscopic imaging with anti-fade performance

In SMLM, a super-resolved image is reconstructed from a time series of frames, each capturing a sparse subset of fluorescently labeled protein targets that can be localized at the single-molecule

level. While SMLM typically achieves higher spatial resolution than PLIM, it requires slower image acquisition. STORM/PALM achieve this sparsity by using photoswitchable fluorophores that stochastically blink on and off. A common PAINT strategy uses dye-conjugated DNA oligonucleotides that transiently hybridize with complementary strands linked to antibody-labeled targets.

We first assessed FLEXTAG in PAINT. FLEXTAG-PAINT offers intrinsic advantages over DNA-PAINT: it does not rely on antibody availability, and its smaller labeling size provides a more accurate representation of protein localization (Fig.7e). Using FLEXTAG ligands conjugated to green (AF488), red (TMR/MaP555), or far red (JF635/HMSiR/AF647) dyes, we obtained three-dimensional (3D) PAINT images for all three FLEXTAG tag/ligand systems, demonstrating that each tag/ligand pair supports self-renewable dynamics compatible with PAINT (Fig.7a-7d). FLEXTAG tag/ligand pairs can also be combined or integrated with established PAINT probes, such as phalloidin-PAINT[35] for actin cytoskeleton imaging, enabling multi-color PAINT imaging. Three-color PAINT imaging enabled direct visualization of the spatial interactions among actin stress fibers, mitochondria, and the ER (Fig. 7f).

We next assessed FLEXTAG in STORM. Unlike PAINT, STORM relies on covalent labeling with photoswitchable dyes or fluorescent proteins, which are prone to photobleaching, limiting long-term imaging of dynamics processes[42]. FLEXTAG-STORM, which uses dynamically exchanging photoswitchable ligands, can overcome this limitation. We used FLEXTAG3 and SLF' as a model system and synthesized a chimeric ligand by conjugating SLF' to HMSiR (a cell-permeable, spontaneously photoswitchable Si-rhodamine dye developed for live-cell STORM[43,44]) (Fig.7g). We first confirmed that SLF'-HMSiR successfully labeled TOM20-

FLEXTAG3-expressing cells (Supplementary Fig.17a). Live-cell FLEXTAG-STORM imaging, acquired at a temporal resolution of 10 seconds, captured dynamic mitochondrial morphology (Fig.7j) and enabled 3D reconstruction (Supplementary Fig.17b). To evaluate anti-fade performance, we compared FLEXTAG3 with slower-renewing precursor tags, $FKBP^{F36V}$ and $FKBP^{F36V, H87A}$, and the non- renewable HaloTag. We monitored the number of single-molecule localizations per image frame at 110 Hz, generating apparent photobleaching curves. FLEXTAG3 retained 96.6 ± 2.3% of single-molecule localizations per frame after ~ 4.5 minutes (30,000 frames), compared to 56.5 ± 3.1%, 48.0 ± 1.1%, and 29.9 ± 5.2% for $FKBP^{F36V}$, $FKBP^{F36V, H87A}$, and HaloTag, respectively (Fig.7h). Furthermore, FLEXTAG3 showed minimal photobleaching in multi-cycle time-lapse live-cell STORM imaging, whereas the other tags exhibited progressive signal loss over time (Fig.7i, 7j, Supplementary Fig.17c). These results demonstrate FLEXTAG-STORM's superior anti-fade performance.

Discussion

We have developed FLEXTAG, a self-renewable protein tagging and labeling framework that enables robust multi-color fluorescence nanoscopy. Through extensive evaluation across multiple nanoscopy modalities with distinct working principles, including SIM, STED, PAINT, and STORM, we demonstrated that FLEXTAG supports 3D multi-color super-resolution imaging in both fixed and live-cell conditions.

While self-renewable tags like dHaloTag[14] (a self-renewable mutant form of HaloTag) and GFP-like chromophore-based renewable protein tags (e.g., pFAST[11]) have been developed, FLEXTAG1, FLEXTAG2, and FLEXTAG3 are distinct in combining self-renewability with a small tag size (~half that of dHaloTag), minimal aggregation, superior apparent photostability

(chromophore-based renewable protein tags suffer from poor photostability and brightness; see Supplementary Fig.1a-1c), and easier expansion to the use of bright organic dyes for multiplexed imaging (chromophore-based renewable protein tags are not easily expandable to other colors because their ligands' fluorescent component is inseparable from the binding motif). Each FLEXTAG tag/ligand system incorporates a dynamic ligand exchange mechanism that enables continuous replenishment of dye-conjugated ligands, maintaining stable fluorescence intensity over extended imaging durations and outperforming HaloTag and the slower-renewing $FKBP^{F36V}$ tag in photobleaching tests. This feature should benefit all nanoscopy techniques examined, where low-brightness fluorophores and photobleaching often compromise image resolution and duration, as well as long-term conventional fluorescence imaging, where extended imaging enables prolonged tracking of protein or organelle dynamics.,

The small size of FLEXTAGs, all under 20 kDa, is crucial for preserving correct protein localization and function. In contrast, the well-known HaloTag, is relatively large (~33 kDa) and mislocalizes proteins, such as COX8, ATP5ME, YTHDC1, and the coronaviral envelope protein. Our three FLEXTAGs preserved proper localization for these proteins, supporting broader applicability for minimally perturbing cellular targets (Supplementary Fig.1d). Moreover, FLEXTAG's small size improves spatial accuracy in imaging by minimizing the dye–target displacement, especially compared to bulky antibody-based methods (~150 kDa for IgGs, ~15 nm span[45])

FLEXTAGs also exhibited minimal aggregation, regardless of ligand presence. Across proteins localized to diverse subcellular compartments, FLEXTAG consistently preserved expected morphology and distribution. This trait is advantageous for both imaging and non-imaging

applications. The precursor proteins of FLEXTAG have previously enabled ligand-inducible manipulations, such as ligand-induced proteolysis of the tagged protein or ligand-induced interactions between tagged proteins. In such contexts, tag-induced aggregation can alter protein localization and function even before the ligand is added to trigger proteolysis or interaction, potentially leading to artifacts or incorrect conclusions. FLEXTAG's minimal aggregation property should improve data reliability in these applications.

As part of our FLEXTAG framework, we developed protective fixation and methods for reducing nonspecific binding of fluorescent ligands, enabling high-quality fixed-cell imaging for self-renewable protein tags. Previous self-renewable protein tags, such as dHaloTag and pFAST, were primarily used for live-cell imaging, largely because fixation often led to greatly reduced labeling efficiencies, resulting in much lower fluorescence intensity. FLEXTAG preserves labeling efficiency and enables higher signal-to-noise ratio imaging. In the future, exploring additional types of blocking agents may help further suppress nonspecific binding. Furthermore, FLEXTAG's compatibility with both live- and fixed-cell imaging makes it promising for applications in correlated light and electron microscopy (CLEM)[42]. In CLEM, live-cell fluorescence imaging visualizes protein dynamics, while electron microscopy (EM), following fixation, reveals ultrastructure of organelles or protein complexes. This combined approach may provide new insights into the relationship between protein complex dynamics and their ultrastructural organization with EM resolutions.

SMLM methods such as STORM and PAINT offer higher spatial resolution than PLIM techniques like SIM and STED, but live-cell SMLM has long been constrained by photobleaching. While dHaloTag has enabled live-cell STED and shows promise for live-cell

SMLM[14], this application has not been demonstrated. Using FLEXTAG-STORM, we achieved prolonged live-cell SMLM imaging with minimal photobleaching while leveraging bright photoswitchable dyes for enhanced spatial resolution (which scales with dye photon output).

Finally, FLEXTAG's "one-for-all" design enables researchers to label proteins once and image them using any of the major nanoscopic techniques, including SIM, STED, PAINT, and STORM, based on experimental requirements. Each technique has distinct strengths and limitations: SMLM offers the highest resolution (1–20 nm) but requires longer acquisition times; STED provides fast imaging with 20–60 nm resolution but demands specialized optics and specific fluorophores; and SIM offers the broadest fluorophore compatibility, albeit with lower resolution (~100–120 nm). Three FLEXTAGs support all three imaging regimes with high orthogonality with minimal crosstalk when co-expressed and co-stained in cells and can flexibly pair with fluorophores across the green, red, and far-red channels, making FLEXTAG a convenient and versatile toolbox and framework for anti-fade multi-color nanoscopic imaging.

In summary, FLEXTAG provides a compact, minimally aggregating, and self-renewable tagging framework compatible with diverse nanoscopy techniques and imaging conditions. Its unique combination of small tag size, superior photostability, bright organic dye compatibility, and orthogonal multiplexing capabilities enables prolonged, high-resolution imaging in both live and fixed cells. By overcoming key limitations of previous renewable tags, FLEXTAG opens new opportunities for visualizing dynamic protein behaviors and deciphering molecular mechanisms with nanoscopic precision, offering broad utility for advancing cell biology and biomedical research.

Data availability

All data supporting the findings of this study are provided within the paper and its Supplementary Information.

Code availability

The following software was used in this study: PyMOL (2.5.4), CellProfiler 4.2.5, and Picasso v0.6.9. Other custom MATLAB codes used in this study are available from the corresponding authors upon reasonable request.

Acknowledgements

This work was supported by the National Institute of General Medical Sciences of the National Institutes of Health (R35GM142973 to R.Z. and R35GM154931 to M.F.), the Life Sciences Research Foundation, and startup funding from the Pennsylvania State University provided to R.Z. We thank Zeyu Xi for helpful discussion regarding HMSiR imaging. We are grateful to Dr. Luke D. Lavis for generously providing HTL-JF630b as a gift. We also acknowledge the Proteomics and Mass Spectrometry Core Facility of the Huck Institutes of the Life Sciences (RRID:SCR_024462) for access to the Bruker UltrafleXtreme MALDI-TOF/TOF instrument.

Author contributions

R.Z. and H.Z. conceived the project, designed the experiments, and interpreted the data. H.Z. and Y.W synthesized the fluorescent ligands. H.Z. and X.W. prepared imaging samples. H.Z. and X.W. performed conventional fluorescence imaging and SMLM imaging experiments. H.Z. performed SIM imaging experiments. H.Z., Y.Y., and M.F. designed and conducted STED imaging experiments. H.Z., Y.T., H.Y., and M.L. developed the software used for data acquisition and analysis. H.Z., X.W., Y.T., and H.Y. analyzed the data. R.Z. and H.Z. wrote the manuscript. R.Z. supervised the project.

Competing interests

R.Z. and H.Z. are co-inventors on a patent application related to this work (US Provisional Patent App No.63/836,663). All other authors declare no competing interests.

References

1. Sigal, Y.M., Zhou, R., and Zhuang, X. (2018). Visualizing and discovering cellular structures with super-resolution microscopy. Science *361*, 880-887. 10.1126/science.aau1044.
2. Fei, J., and Zhou, R. (2023). Watching biomolecules stride in real time. Science *379*, 986-987. doi:10.1126/science.adg8451.
3. Rust, M.J., Bates, M., and Zhuang, X. (2006). Sub-diffraction-limit imaging by stochastic optical reconstruction microscopy (STORM). Nature methods *3*, 793-796.
4. Betzig, E., Patterson, G.H., Sougrat, R., Lindwasser, O.W., Olenych, S., Bonifacino, J.S., Davidson, M.W., Lippincott-Schwartz, J., and Hess, H.F. (2006). Imaging intracellular fluorescent proteins at nanometer resolution. science *313*, 1642-1645.
5. Schnitzbauer, J., Strauss, M.T., Schlichthaerle, T., Schueder, F., and Jungmann, R. (2017). Super-resolution microscopy with DNA-PAINT. Nature protocols *12*, 1198-1228.
6. Zhang, M., Chang, H., Zhang, Y., Yu, J., Wu, L., Ji, W., Chen, J., Liu, B., Lu, J., and Liu, Y. (2012). Rational design of true monomeric and bright photoactivatable fluorescent proteins. Nature methods *9*, 727-729.
7. Wang, S., Moffitt, J.R., Dempsey, G.T., Xie, X.S., and Zhuang, X. (2014). Characterization and development of photoactivatable fluorescent proteins for single-molecule–based superresolution imaging. Proceedings of the National Academy of Sciences *111*, 8452-8457.
8. Los, G.V., Encell, L.P., McDougall, M.G., Hartzell, D.D., Karassina, N., Zimprich, C., Wood, M.G., Learish, R., Ohana, R.F., and Urh, M. (2008). HaloTag: a novel protein labeling technology for cell imaging and protein analysis. ACS chemical biology *3*, 373-382.
9. Gautier, A., Juillerat, A., Heinis, C., Corrêa, I.R., Kindermann, M., Beaufils, F., and Johnsson, K. (2008). An engineered protein tag for multiprotein labeling in living cells. Chemistry & biology *15*, 128-136.
10. Keppler, A., Gendreizig, S., Gronemeyer, T., Pick, H., Vogel, H., and Johnsson, K. (2003). A general method for the covalent labeling of fusion proteins with small molecules in vivo. Nature biotechnology *21*, 86-89.
11. Benaissa, H., Ounoughi, K., Aujard, I., Fischer, E., Goïame, R., Nguyen, J., Tebo, A.G., Li, C., Le Saux, T., and Bertolin, G. (2021). Engineering of a fluorescent chemogenetic reporter with tunable color for advanced live-cell imaging. Nature Communications *12*, 6989.
12. Muslinkina, L., Gavrikov, A.S., Bozhanova, N.G., Mishin, A.S., Baranov, M.S., Meiler, J., Pletneva, N.V., Pletnev, V.Z., and Pletnev, S. (2020). Structure-based rational design of two enhanced bacterial lipocalin Blc tags for protein-PAINT super-resolution microscopy. ACS Chemical Biology *15*, 2456-2465.
13. Liu, W., Li, F., Chen, X., Hou, J., Yi, L., and Wu, Y.-W. (2014). A rapid and fluorogenic TMP-AcBOPDIPY probe for covalent labeling of proteins in live cells. Journal of the American Chemical Society *136*, 4468-4471.
14. Kompa, J., Bruins, J., Glogger, M., Wilhelm, J., Frei, M.S., Tarnawski, M., D'Este, E., Heilemann, M., Hiblot, J., and Johnsson, K. (2023). Exchangeable HaloTag ligands for super-resolution fluorescence microscopy. Journal of the American Chemical Society *145*, 3075-3083.

15. Pearson, G.J., Mears, H.V., Broncel, M., Snijders, A.P., Bauer, D.L., and Carlton, J.G. (2024). ER-export and ARFRP1/AP-1–dependent delivery of SARS-CoV-2 Envelope to lysosomes controls late stages of viral replication. Science Advances *10*, eadl5012.
16. Bond, A.G., Craigon, C., Chan, K.-H., Testa, A., Karapetsas, A., Fasimoye, R., Macartney, T., Blow, J.J., Alessi, D.R., and Ciulli, A. (2021). Development of BromoTag: a "Bump-and-Hole"–PROTAC system to induce potent, rapid, and selective degradation of tagged target proteins. *64*, 15477-15502.
17. Filippakopoulos, P., Qi, J., Picaud, S., Shen, Y., Smith, W.B., Fedorov, O., Morse, E.M., Keates, T., Hickman, T.T., and Felletar, I. (2010). Selective inhibition of BET bromodomains. Nature *468*, 1067-1073.
18. Vollmuth, F., Blankenfeldt, W., and Geyer, M. (2009). Structures of the dual bromodomains of the P-TEFb-activating protein Brd4 at atomic resolution. Journal of Biological Chemistry *284*, 36547-36556.
19. Mirdita, M., Schütze, K., Moriwaki, Y., Heo, L., Ovchinnikov, S., and Steinegger, M. (2022). ColabFold: making protein folding accessible to all. Nature methods *19*, 679-682.
20. Nakamura, Y., Umehara, T., Nakano, K., Jang, M.K., Shirouzu, M., Morita, S., Uda-Tochio, H., Hamana, H., Terada, T., and Adachi, N. (2007). Crystal structure of the human BRD2 bromodomain: insights into dimerization and recognition of acetylated histone H4. Journal of Biological Chemistry *282*, 4193-4201.
21. Miller, L.W., Cai, Y., Sheetz, M.P., and Cornish, V.W. (2005). In vivo protein labeling with trimethoprim conjugates: a flexible chemical tag. Nature methods *2*, 255-257.
22. Chen, Z., Jing, C., Gallagher, S.S., Sheetz, M.P., and Cornish, V.W. (2012). Second-generation covalent TMP-tag for live cell imaging. Journal of the American Chemical Society *134*, 13692-13699.
23. Mo, J., Chen, J., Shi, Y., Sun, J., Wu, Y., Liu, T., Zhang, J., Zheng, Y., Li, Y., and Chen, Z. (2022). Third-Generation Covalent TMP-Tag for Fast Labeling and Multiplexed Imaging of Cellular Proteins. Angewandte Chemie *134*, e202207905.
24. Takahashi, H., Yokota, A., Takenawa, T., and Iwakura, M. (2009). Sequence perturbation analysis: addressing amino acid indices to elucidate the C-terminal role of Escherichia coli dihydrofolate reductase. Journal of biochemistry *145*, 751-762.
25. Ainavarapu, S.R.K., Li, L., Badilla, C.L., and Fernandez, J.M. (2005). Ligand binding modulates the mechanical stability of dihydrofolate reductase. Biophysical journal *89*, 3337-3344.
26. Tian, J., Woodard, J.C., Whitney, A., and Shakhnovich, E.I. (2015). Thermal stabilization of dihydrofolate reductase using monte carlo unfolding simulations and its functional consequences. PLoS computational biology *11*, e1004207.
27. Villafranca, J.E., Howell, E.E., Oatley, S.J., Xuong, N.H., and Kraut, J. (1987). An engineered disulfide bond in dihydrofolate reductase. Biochemistry *26*, 2182-2189.
28. Sirawaraporn, W., Prapunwattana, P., Sirawaraporn, R., Yuthavong, Y., and Santi, D. (1993). The dihydrofolate reductase domain of Plasmodium falciparum thymidylate synthase-dihydrofolate reductase. Gene synthesis, expression, and anti-folate-resistant mutants. Journal of biological chemistry *268*, 21637-21644.
29. Marks, K.M., Braun, P.D., and Nolan, G.P. (2004). A general approach for chemical labeling and rapid, spatially controlled protein inactivation. Proceedings of the National Academy of Sciences *101*, 9982-9987.

30. Clackson, T., Yang, W., Rozamus, L.W., Hatada, M., Amara, J.F., Rollins, C.T., Stevenson, L.F., Magari, S.R., Wood, S.A., and Courage, N.L. (1998). Redesigning an FKBP–ligand interface to generate chemical dimerizers with novel specificity. Proceedings of the National Academy of Sciences *95*, 10437-10442.
31. Kolos, J.M., Voll, A.M., Bauder, M., and Hausch, F. (2018). FKBP ligands—where we are and where to go? Frontiers in pharmacology *9*, 1425.
32. Du, Z., Wang, W., Luo, S., Zhang, L., Yuan, S., Hei, Y., Bao, Z., Chen, C., Lin, Y., and Chu, L. (2023). Self-renewable tag for photostable fluorescence imaging of proteins. Journal of the American Chemical Society *145*, 18968-18976.
33. Richter, K.N., Revelo, N.H., Seitz, K.J., Helm, M.S., Sarkar, D., Saleeb, R.S., d'Este, E., Eberle, J., Wagner, E., and Vogl, C. (2018). Glyoxal as an alternative fixative to formaldehyde in immunostaining and super-resolution microscopy. The EMBO journal *37*, 139-159.
34. Sabatini, D.D., Bensch, K., and Barrnett, R.J. (1963). Cytochemistry and electron microscopy: the preservation of cellular ultrastructure and enzymatic activity by aldehyde fixation. The Journal of cell biology *17*, 19-58.
35. Gunasekara, H., Perera, T., Chao, C.-J., Bruno, J., Saed, B., Anderson, J., Zhao, Z., and Hu, Y.S. (2024). Phalloidin-PAINT: Enhanced quantitative nanoscale imaging of F-actin. Biophysical Journal *123*, 3051-3064.
36. Zanetti-Domingues, L.C., Tynan, C.J., Rolfe, D.J., Clarke, D.T., and Martin-Fernandez, M. (2013). Hydrophobic fluorescent probes introduce artifacts into single molecule tracking experiments due to non-specific binding. PloS one *8*, e74200.
37. Grimm, J.B., Muthusamy, A.K., Liang, Y., Brown, T.A., Lemon, W.C., Patel, R., Lu, R., Macklin, J.J., Keller, P.J., and Ji, N. (2017). A general method to fine-tune fluorophores for live-cell and in vivo imaging. Nature methods *14*, 987-994.
38. Zheng, Q., Ayala, A.X., Chung, I., Weigel, A.V., Ranjan, A., Falco, N., Grimm, J.B., Tkachuk, A.N., Wu, C., and Lippincott-Schwartz, J. (2019). Rational design of fluorogenic and spontaneously blinking labels for super-resolution imaging. ACS Central Science *5*, 1602-1613.
39. Miller, L.W., Sable, J., Goelet, P., Sheetz, M.P., and Cornish, V.W. (2004). Methotrexate conjugates: a molecular in vivo protein tag. Angewandte Chemie-International Edition *43*, 1672-1675.
40. Carroll, M.J., Mauldin, R.V., Gromova, A.V., Singleton, S.F., Collins, E.J., and Lee, A.L. (2012). Evidence for dynamics in proteins as a mechanism for ligand dissociation. Nature chemical biology *8*, 246-252.
41. Wang, L., Tran, M., D'Este, E., Roberti, J., Koch, B., Xue, L., and Johnsson, K. (2020). A general strategy to develop cell permeable and fluorogenic probes for multicolour nanoscopy. Nature Chemistry *12*, 165-172.
42. Arizono, M., Idziak, A., Quici, F., and Nägerl, U.V. (2023). Getting sharper: the brain under the spotlight of super-resolution microscopy. Trends in cell biology *33*, 148-161.
43. Uno, S.-n., Kamiya, M., Yoshihara, T., Sugawara, K., Okabe, K., Tarhan, M.C., Fujita, H., Funatsu, T., Okada, Y., and Tobita, S. (2014). A spontaneously blinking fluorophore based on intramolecular spirocyclization for live-cell super-resolution imaging. Nature chemistry *6*, 681-689.

44. Grimm, J.B., English, B.P., Chen, J., Slaughter, J.P., Zhang, Z., Revyakin, A., Patel, R., Macklin, J.J., Normanno, D., and Singer, R.H. (2015). A general method to improve fluorophores for live-cell and single-molecule microscopy. Nature methods *12*, 244-250.
45. Lin, H.-H., Wang, C.-H., Huang, S.-H., Lin, S.-Y., Kato, T., Namba, K., Hosogi, N., Song, C., Murata, K., and Yen, C.-H. (2024). Use of phase plate cryo-EM reveals conformation diversity of therapeutic IgG with 50 kDa Fab fragment resolved below 6 Å. Scientific Reports *14*, 14079.
46. Holland, K.L., Plutkis, S.E., Daugird, T.A., Sau, A., Grimm, J.B., English, B.P., Zheng, Q., Dave, S., Rahman, F., and Xie, L. (2024). A series of spontaneously blinking dyes for super-resolution microscopy. bioRxiv.

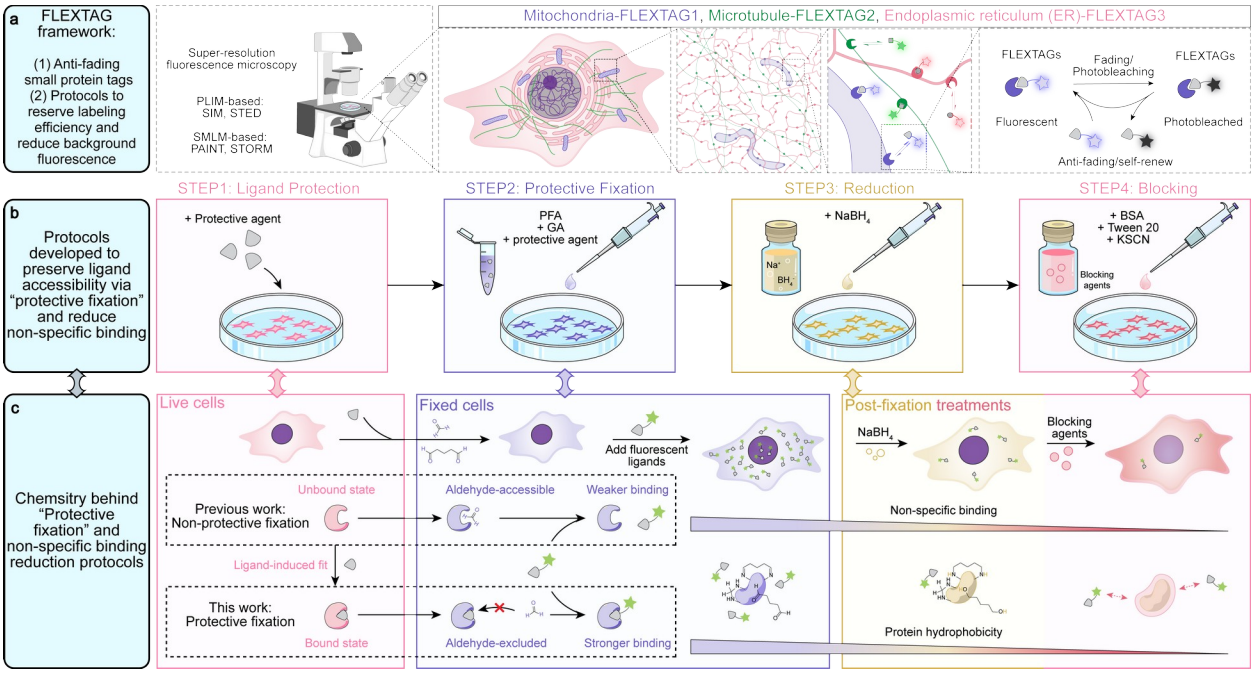

Fig.1. Overall scheme of the FLEXTAG framework.

a, The developed FLEXTAG framework comprises three orthogonal, compact, and self-renewable (anti-fading) protein tags, along with optimized protocols designed to enhance labeling efficiency and reduce background fluorescence. Self-renewal allows photobleached fluorophores to be replaced by fresh fluorophores thereby restoring fluorescent signals. **b,** Schematic overview of the 4-step protocol designed to preserve ligand accessibility via "protective fixation" and reduce non-specific binding. Step 1: Preincubate cells expressing FLEXTAGs with a high-concentration of dye-free binding moieties of the FLEXTAG ligands, used as a protective agent. Step 2: Fix cells with an aldehyde-based fixative containing the same concentration as the protective agents. Step 3: Quench excess aldehydes with $NaBH_4$. Step 4: Block fixed protein surfaces with a combination of BSA, Tween-20, and KSCN, identified as effective blocking agents. **c,** Chemical basis behind "Protective fixation" and nonspecific binding reduction strategies. Step 1: Preincubation with the dye-free binding moieties of the FLEXTAG ligand locks each tag into its ligand-bound conformation. Step 2: Occupation of the binding pockets shields reactive residues from crosslinking by aldehyde fixatives, thereby preserving ligand accessibility. Step 3: Residual aldehydes on protein surfaces are reduced to alcohols by $NaBH_4$ decreasing surface hydrophobicity and reducing nonspecific binding of fluorescent ligands. Step 4: Blocking agents further modulate the microenvironment of fixed protein surfaces to suppress remaining nonspecific interactions.

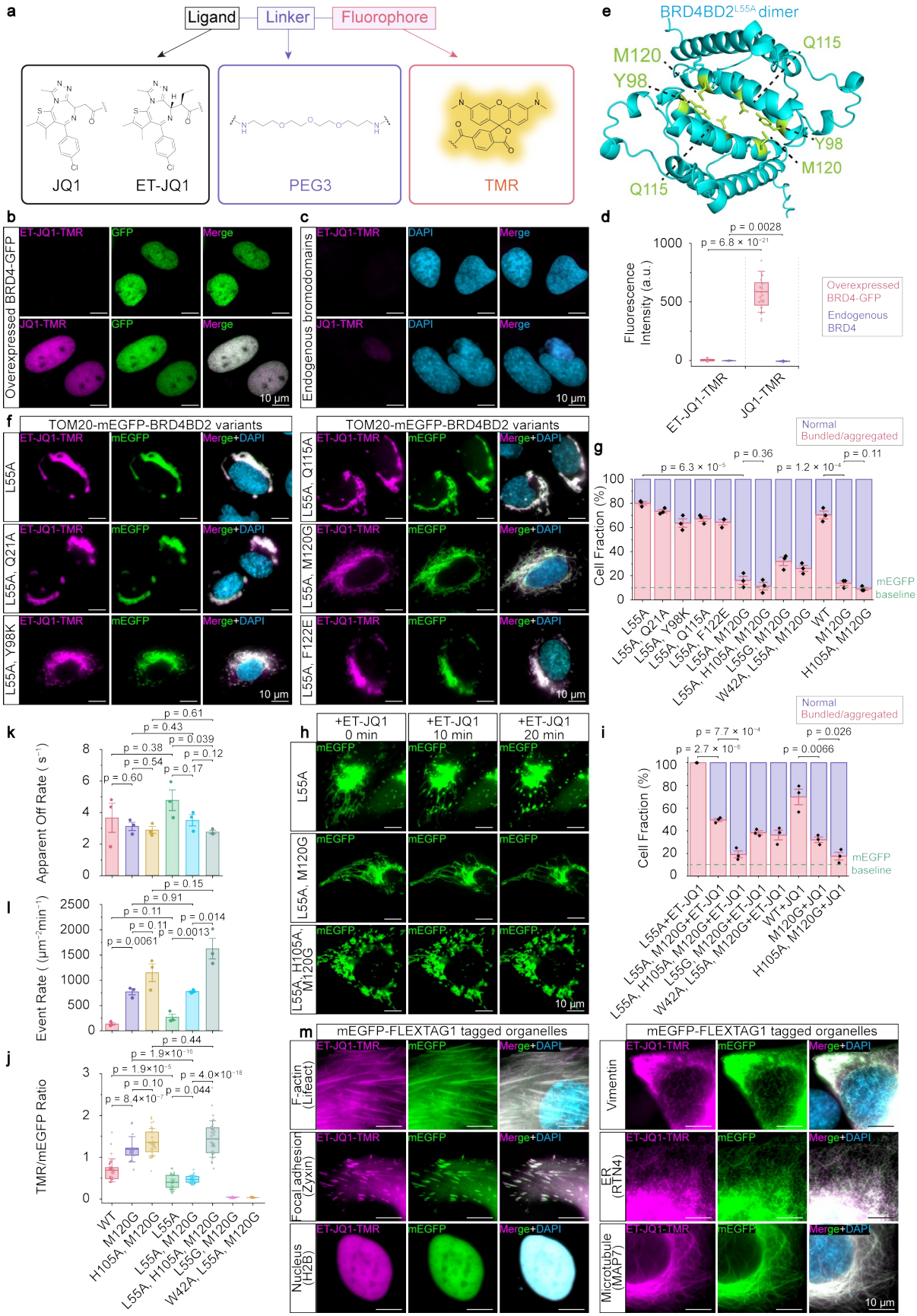
a
Ligand
Linker
Fluorophore
JQ1
ET-JQ1
PEG3
TMR
b
Overexpressed BRD4-GFP
ET-JQ1-TMR
GFP
Merge
JQ1-TMR
10 μm
c
Endogenous bromodomains
DAPI
d
Fluorescence Intensity (a.u.)
p = 0.0028
p = 6.8 × 10⁻²¹
Overexpressed BRD4-GFP
Endogenous BRD4
e
BRD4BD2L55A dimer
M120
Y98
Q115
f
TOM20-mEGFP-BRD4BD2 variants
mEGFP
Merge+DAPI
L55A
L55A, Q21A
L55A, Y98K
L55A, Q115A
L55A, M120G
L55A, F122E
g
Normal
Bundled/aggregated
Cell Fraction (%)
p = 6.3 × 10⁻⁵
p = 0.36
p = 1.2 × 10⁻⁴
p = 0.11
mEGFP baseline
WT
H105A, M120G
h
+ET-JQ1 0 min
+ET-JQ1 10 min
+ET-JQ1 20 min
i
p = 7.7 × 10⁻⁴
p = 2.7 × 10⁻⁶
p = 0.026
p = 0.0066
L55A+ET-JQ1
L55A, M120G+ET-JQ1
L55A, H105A, M120G+ET-JQ1
L55G, M120G+ET-JQ1
W42A, L55A, M120G+ET-JQ1
WT+JQ1
M120G+JQ1
H105A, M120G+JQ1
j
TMR/mEGFP Ratio
p = 1.9×10⁻¹⁶
p = 1.9×10⁻⁵
p = 0.10
p = 8.4×10⁻⁷
p = 4.0×10⁻¹⁸
p = 0.044
k
Apparent Off Rate (s⁻¹)
p = 0.61
p = 0.43
p = 0.039
p = 0.38
p = 0.12
p = 0.54
p = 0.17
p = 0.60
l
Event Rate ((μm⁻²min⁻¹)
p = 0.15
p = 0.91
p = 0.11
p = 0.014
p = 0.11
p = 0.0013
p = 0.0061
m
mEGFP-FLEXTAG1 tagged organelles
F-actin (Lifeact)
Focal adhesion (Zyxin)
Nucleus (H2B)
Vimentin
ER (RTN4)
Microtubule (MAP7)

Fig.2. Development and characterization of FLEXTAG1.
a, Chemical structures of ligand-linker-fluorophore conjugates targeting BRD4BD2^{WT} or BRD4BD2^{L55A}. **b,** Representative -epi-fluorescence images of GFP-tagged full length BRD4 (BRD4-GFP), labeled with 1 μM ET-JQ1-TMR or JQ1-TMR. Scale bars: 10 μm. **c,** Representative epi-fluorescence images of endogenous bromodomain proteins, labeled by 1 μM ET-JQ1-TMR or JQ1-TMR and 1 μg/mL DAPI. Scale bars: 10 μm. **d,** Quantification of ET-JQ1-TMR or JQ1-TMR fluorescence intensity in cells overexpressing BRD4-GFP or endogenous bromodomain proteins. Each data point represents the average TMR signal within a GFP- or DAPI-masked nuclear region from a single field of view. **e,** ColabFold-predicted dimer interface of BRD4BD2^{L55A}. Key inter-protein interactions are highlighted in green, including Y98-M120 and Q115-Q115. **f,** Representative epi-fluorescence images of TOM20-mEGFP-BRD4BD2^{L55A} variants. All mutations retain binding capability to ET-JQ1-TMR. Scale bars: 10 μm. **g,** Quantification of the fraction of cells overexpressing TOM20-mEGFP-BRD4BD2 variants showing normal versus bundled/aggregated mitochondrial morphology. Cells overexpressing TOM20-mEGFP, which does not dimerize, served as the monomeric baseline control (dashed green line). **h,** Representative epi-fluorescence images of mitochondrial morphology in cells overexpressing TOM20-mEGFP-BRD4BD2 variants at 0, 10, and 20 minutes after the addition of 100 μM ET-JQ1. Scale bars: 10 μm. **i,** Same as **g**, except the mitochondrial morphology was assessed 1 hour after the addition of 100 μM ET-JQ1. **j,** Quantification of the TMR/mEGFP fluorescence ratio following labeling of cells expressing TOM20-mEGFP-BRD4BD2 variants with 1 μM ET-JQ1-TMR. Each data point represents the average TMR/mEGFP ratio of mEGFP-masked regions in a single field of view. **k,** Quantification of apparent off rates for 1 nM ET-JQ1 or JQ1-TMR binding to TOM20-mEGFP-BRD4BD2 variants in fixed cells, based on single-molecule localization microscopy (SMLM) movies (10,000 frames, 10 Hz). Data are presented as mean ± SEM (N = 3 independent experiments). **l,** Same as **k**, but quantifying binding event rates. **m,** Representative epi-fluorescence images of BRD4BD2$^{L55A,\ H105A,\ M120G}$ (FLEXTAG1)-tagged cellular structures. Samples were labeled with 1 μM ET-JQ1-TMR or JQ1-TMR and 1μg/mL DAPI. Scale bars: 10 μm.

Boxplots show the mean and boundaries (first and third quartiles), and the whiskers denote SD. p-values calculated with two-sided unpaired Student's t-test.

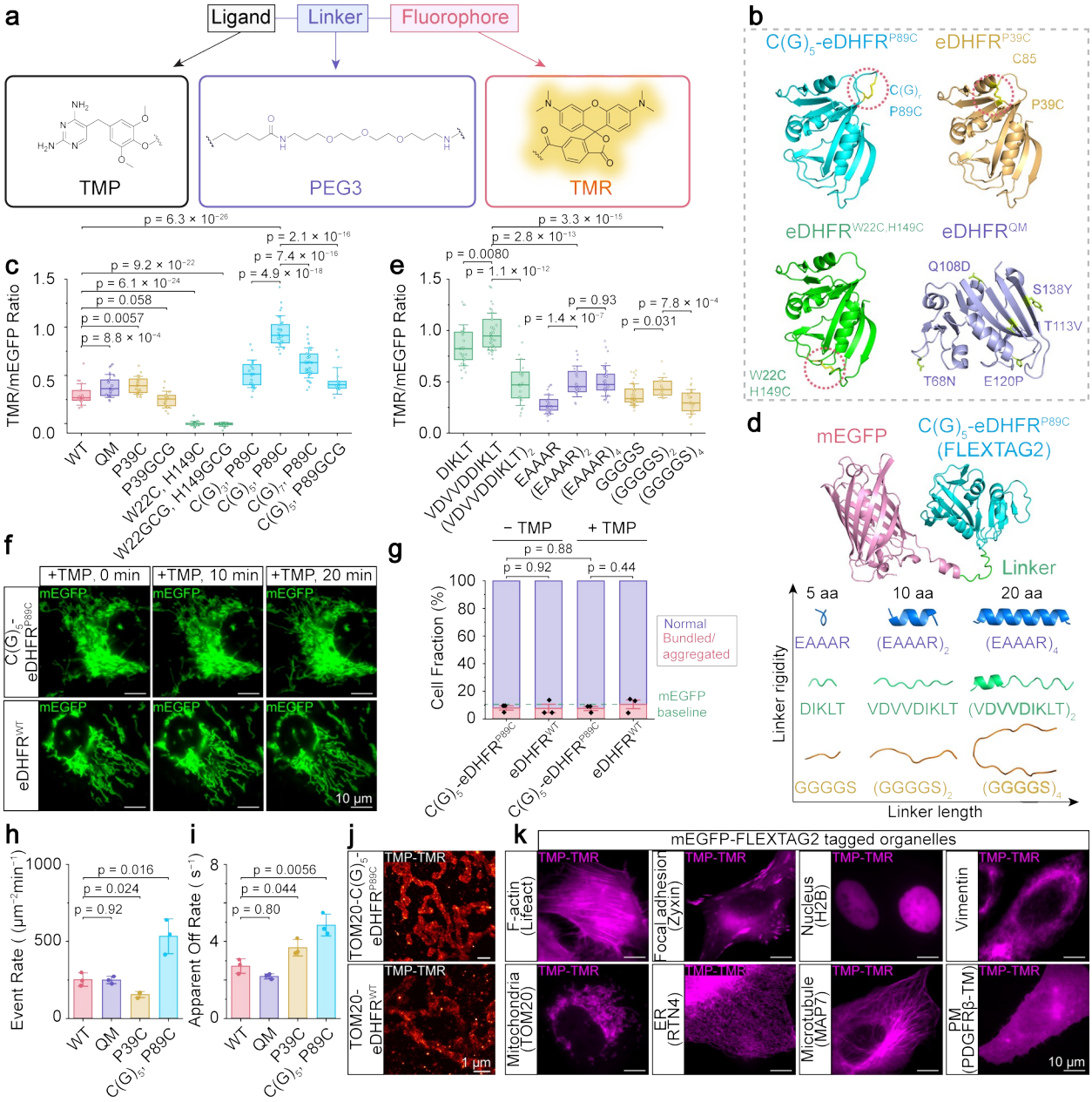

Fig.3. Development and characterization of FLEXTAG2.

a, Chemical structures of ligand-linker-fluorophore conjugates targeting eDHFR. **b,** ColabFold-predicted structures of eDHFR variants. Designed intramolecular disulfide bonds (yellow) in $C(G)_5$-eDHFR^{P89C}, eDHFR^{P39C}, and eDHFR$^{W22C,\ H149C}$ are highlighted with red circles. Thermally stabilizing mutations in eDHFR^{QM} are shown in green. **c,** Quantification of the TMR/mEGFP fluorescence ratio in cells overexpressing TOM20-mEGFP-eDHFR variants labeled with 1 μM TMP-TMR. Each data point represents the average TMR/mEGFP ratio of mEGFP-masked regions in a single field of view. Boxplots show the mean and boundaries (first and third quartiles); whiskers denote SD. p-values calculated with two-sided unpaired Student's t-test. **d,** ColabFold-predicted structures of mEGFP-(VDVVDDIKLT)-$C(G)_5$-eDHFR^{P89C} (FLEXTAG2) and designs of linkers inserted between mEGFP and eDHFR variants. Linkers of varying lengths

(5, 10, or 20 amino acids) and rigidity (rigid, moderately flexible, or flexible, based on the predicted confidence of stable α-helix formation) were screened. **e,** Same as **c** but quantifying cells overexpressing TOM20-mEGFP-(designed linkers)-C$(G)_5$-eDHFR^{P89C}. **f,** Representative epi-fluorescence images showing mitochondrial morphology in cells overexpressing TOM20-mEGFP-C$(G)_5$-eDHFR^{P89C} or TOM20-mEGFP-eDHFR^{WT} at 0, 10, and 20 minutes after the addition of 100 μM TMP. Scale bars: 10 μm. **g,** Quantification of the fraction of cells overexpressing TOM20-mEGFP-C$(G)_5$-eDHFR^{P89C} or TOM20-mEGFP-eDHFR^{WT} showing normal versus bundled/aggregated mitochondrial morphology, in the absence or 1 hour after the addition of 100 μM TMP. The baseline fraction of cells overexpressing TOM20-mEGFP that exhibit bundled/aggregated mitochondria is indicated by the green dashed line. **h,** Quantification of binding event rates for 1 nM TMP-TMR binding to TOM20-mEGFP-eDHFR variants in fixed cells, based on single-molecule localization microscopy (SMLM) movies (10,000 frames, 10 Hz). Each data point represents the average number of localizations per μm^2 per minute for one cell. Data are presented as mean ± SEM (N = 3 independent experiments). p-values calculated with two-sided unpaired Student's t-test. **i,** Same as **h** but for quantifying apparent off rates. **j,** Representative PAINT images of TOM20-mEGFP-C$(G)_5$-eDHFR^{P89C} and TOM20-mEGFP-eDHFR^{WT}, imaged with 1 nM TMP-TMR in fixed cells. Scale bars: 1 μm. **k,** Representative epi-fluorescence images of C$(G)_5$-eDHFR^{P89C} (FLEXTAG2)-tagged cellular structures, labeled with 1 μM TMP-TMR. Scale bars: 10 μm.

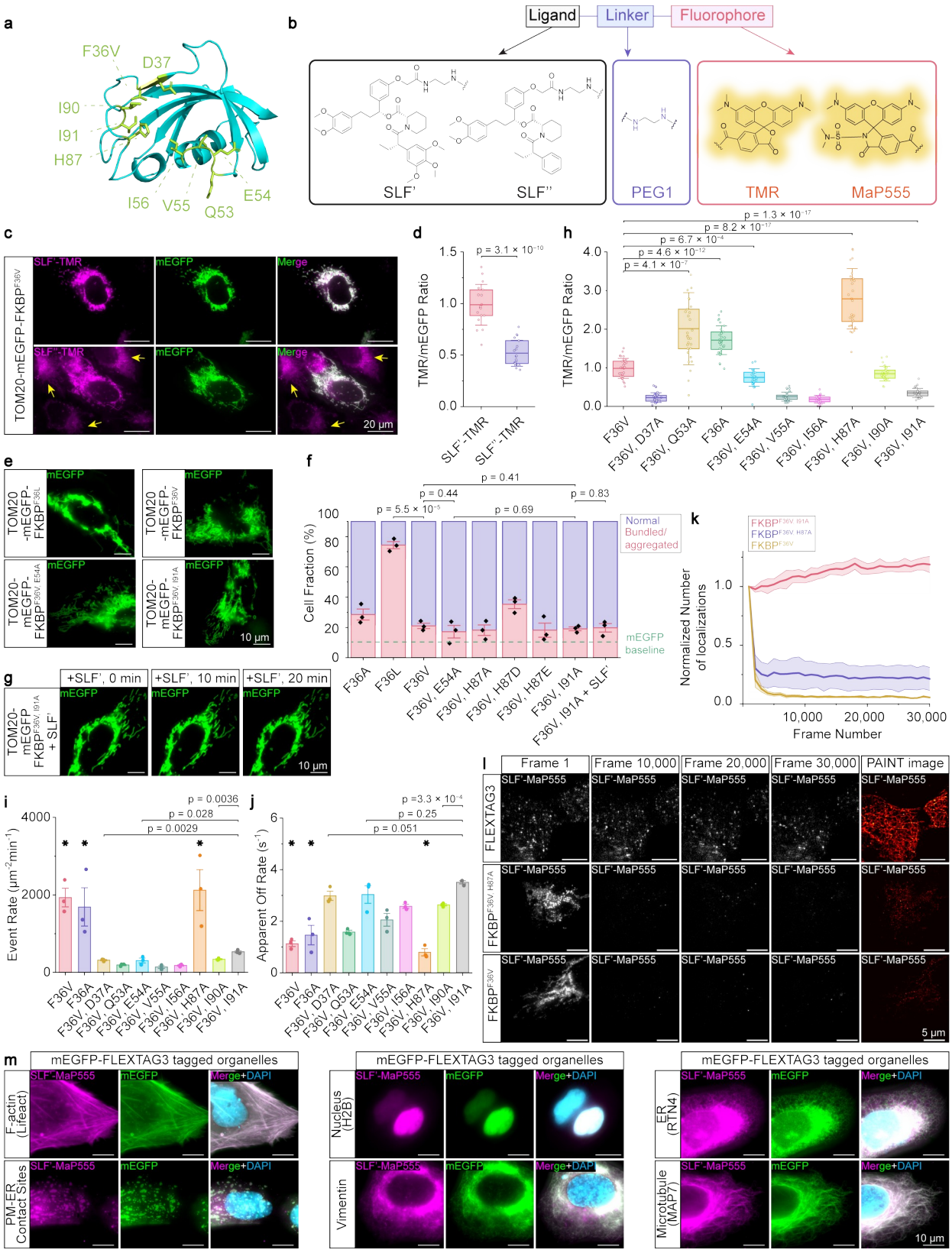

Fig.4. Development and characterization of FLEXTAG3.

a, ColabFold-predicted structure of $FKBP^{F36V}$ aligned with the reported co-crystal structure of $FKBP^{F36V}$ and SLF' (PDB: 1BL4). Amino acids near the ligand binding pocket potentially affecting exchange kinetics are highlighted in green, including D37, Q53, E54, V55, I56, H87, I90, and I91. **b,** Chemical structures of ligand-linker-fluorophore conjugates targeting FKBP variants. **c,** Representative epi-fluorescence images of TOM20-mEGFP-$FKBP^{F36V}$labeled with 1 µM SLF'-TMR or SLF''-TMR. SLF'-TMR shows high selectivity for $FKBP^{F36V}$, whereas SLF''-TMR exhibits fluorescence signals in cells lacking $FKBP^{F36V}$ expression. Yellow arrowheads indicate non-specific binding in untransfected cells. Scale bars: 20 µm. **d,** Quantification of TMR/mEGFP fluorescence ratios in cells overexpressing $FKBP^{F36V}$ labeled with 1 µM SLF'-TMR or SLF''-TMR. Each data point represents the average TMR/mEGFP ratio of mEGFP-masked regions in a single field of view. **e,** Representative images of mitochondrial morphology in cells overexpressing TOM20-mEGFP-FKBP variants. Scale bars: 10 µm. **f,** Quantification of the fraction of cells overexpressing TOM20-mEGFP-FKBP variants showing normal versus bundled/aggregated mitochondria. The baseline fraction of cells overexpressing TOM20-mEGFP that exhibit bundled/aggregated mitochondria is indicated by the green dashed line. **g,** Representative epi-fluorescence images showing mitochondrial morphology in cells overexpressing TOM20-mEGFP-$FKBP^{F36V, I91A}$ at 0, 10, and 20 minutes after the addition of 100 µM SLF'. Scale bars: 10 µm. **h,** Quantification of the TMR/mEGFP fluorescence ratio in cells overexpressing TOM20-mEGFP-FKBP variants labeled with 1 µM SLF'-TMR. Each data point represents the average TMR/mEGFP ratio of mEGFP-masked region in a single field of view. **i,** Quantification of binding event rates for 100 pM SLF'-MaP555 binding to TOM20-mEGFP-FKBP variants in fixed cells, based on single-molecule localization microscopy (SMLM) movies (10,000 frames, 10 Hz). Each data point represents the average number of localizations per μm^2 per minute for one cell. Three independent experiments were performed for each FKBP variant. Mutations with prolonged binding durations, where photobleaching often precedes dissociation, potentially leading to inaccurate kinetic measurements, are marked with asterisks. Data are presented as mean ± SEM (N = 3 independent experiments). **j,** Same as **i**, except for quantifying apparent off rates. **k,** Quantification of the survival rate of the single-molecule localizations during 30,000-frame PAINT imaging of 1 nM SLF'-MaP555 binding to $FKBP^{F36V, I91A}$, $FKBP^{F36V, H87A}$, and $FKBP^{F36V}$ in fixed cells. Localization numbers per frame were normalized to the first frame. Data are presented as mean ± SEM (N = 3 independent experiments). **l,** Representative images at frames 1, 10,000, 20,000, 30,000, and reconstructed PAINT images of $FKBP^{F36V, I91A}$ (FLEXTAG3), $FKBP^{F36V, H87A}$, and $FKBP^{F36V}$. Scale bars: 5 µm. **m,** Representative epi-fluorescence images of $FKBP^{F36V, I91A}$ (FLEXTAG3)-tagged cellular structures. Samples were labeled with 1 µM SLF'-MaP555 and 1µg/mL DAPI. Scale bars: 10 µm.

Boxplots show the mean and boundaries (first and third quartiles); whiskers denote SD. p-values calculated with two-sided unpaired Student's t-test.

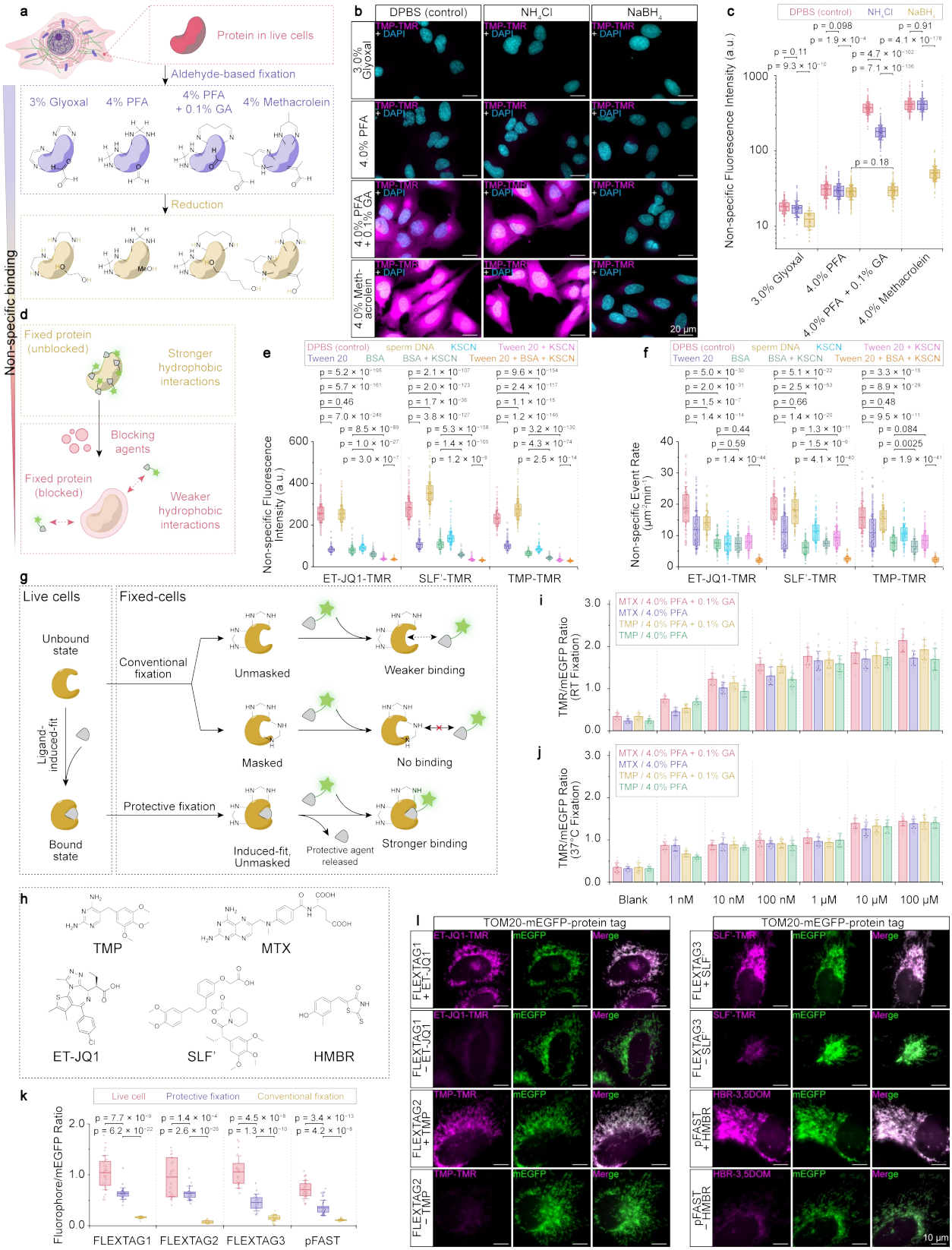

Fig.5. Strategies to reduce non-specific binding and enable protective fixation.

a, Schematic of chemical reactions occurring on protein surfaces during fixation and the subsequent reduction. Increased surface hydrophobicity of fixed proteins, resulting from crosslink formation and residual aldehydes, are reduced by reducing agents, such as NH_4Cl or $NaBH_4$. **b,** Representative epi-fluorescence images showing non-specific binding in fixed cells. Cells were fixed with indicated fixatives, followed by treatment with DPBS (control), 50 mM NH_4Cl in DPBS, or 50 mM $NaBH_4$ in DPBS. Imaging was performed using 20 nM TMP-TMR in DPBS without washing. Scale bars: 20 μm. **c,** Quantification of non-specific TMP-TMR fluorescence intensity. Each data point represents the average fluorescence intensity of a single cell. **d,** Schematic illustrating the blocking effects of various agents on fixed protein surface, which alter the local microenvironment on the fixed protein surfaces and thereby reduces non-specific binding of ligand-linker-fluorophore conjugates. **e,** Quantification of non-specific fluorescence intensity of ET-JQ1-TMR, SLF'-TMR, or TMP-TMR in cells fixed with 4.0% PFA + 0.1% GA, followed by reduction with 50 mM $NaBH_4$ in DPBS. Cells were imaged in 1) DPBS (control); 2) 0.1% Tween 20 (detergent-based blocking agent); 3) 100 μg/mL sperm DNA (nucleotide-based blocking agent); 4) 3.0% BSA (protein-based blocking agent); 5) 300 mM potassium thiocyanate (chaotropic ion); 6) 3.0% BSA + 300 mM KSCN; 7) 0.1% Tween-20 + 300 mM KSCN; 8) 3.0% BSA + 0.1% Tween-20 + 300 mM KSCN . Each data point represents the average fluorescence intensity of a single cell. **f,** Quantification of non-specific binding event rate for 1 nM ET-JQ1-TMR/SLF'-TMR/TMP-TMR in fixed cells, based on single-molecule localization microscopy (SMLM) movies (10,000 frames, 10 Hz). Data points in each box were obtained from three independent experiments, each on a different cell. ~30 randomly selected circular regions (1.6 μm diameter) were analyzed. **g,** Schematic of "protective fixation". Pre-incubation with protective ligands prior to fixation shields binding pockets from aldehyde-induced modification and locks the protein tag in its ligand-induced-fit conformation. **h,** Chemical structures of protective agents, including ET-JQ1 for FLEXTAG1, TMP and MTX for FLEXTAG2, SLF' for FLEXTAG3, and HMBR for pFAST. **i,** Quantification of the TMR/mEGFP fluorescence ratio in fixed cells overexpressing TOM20-mEGFP-FLEXTAG2 labeled with 20 nM TMP-TMR. Protective agents TMP/MTX (0–100 μM) were added to the culture medium 1 or 12 hours prior to fixation to allow cellular uptake, followed by fixation with 4.0% PFA or 4.0% PFA + 0.1% GA at room temperature, and imaged with 20 nM TMP-TMR to calculate the TMR/mEGFP ratio. Each data point represents the average TMR/mEGFP ratio of mEGFP-masked regions in a single field of view. **j,** Quantification of TMR/mEGFP fluorescence ratio in fixed cells. Cells were fixed at 37 °C. Boxplots show the mean and boundaries (first and third quartiles); whiskers denote SD. **k,** Comparison of the fluorophore (ET-JQ1-TMR/TMP-TMR/SLF'-TMR/HBR-3,5DOM)/mEGFP ratio in live cells, cells fixed by protective fixation, and cells fixed by conventional fixation without protection. Each data point represents the average fluorophore/mEGFP ratio of mEGFP-masked regions in a single field of view. Boxplots show the mean and boundaries (first and third quartiles); whiskers denote SD. **l,** Representative epi-fluorescence images comparing protective fixation and conventional fixation for FLEXTAG1, FLEXTAG2, FLEXTAG3, and pFAST. Scale bars: 10 μm.

Boxplots show the mean and boundaries (first and third quartiles); whiskers denote SD. p-values calculated with two-sided unpaired Student's t-test.

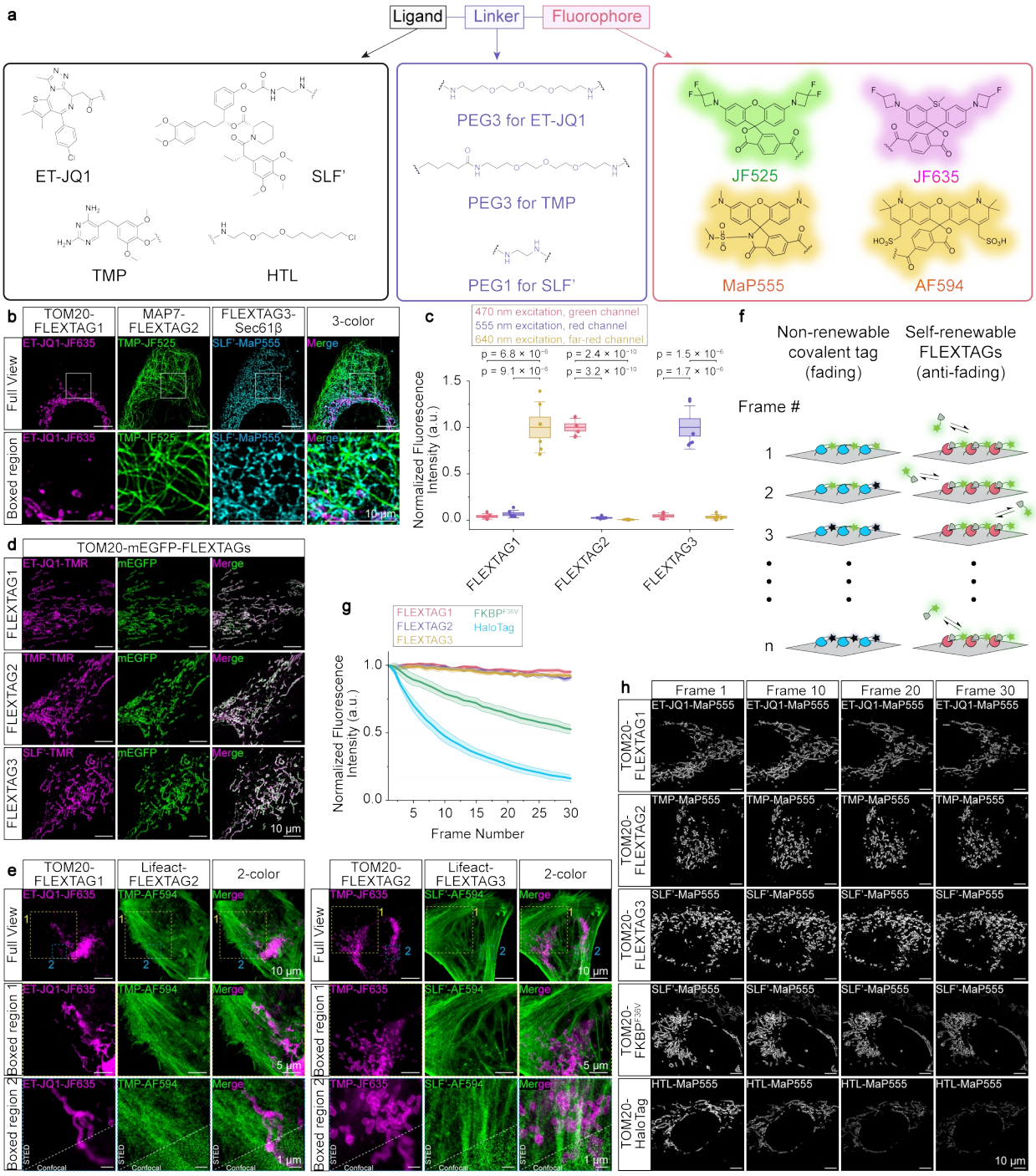

Fig.6. FLEXTAG enables PLIM-based nanoscopic imaging with anti-fade performance. **a,** Chemical structures of ligand-linker-fluorophore conjugates targeting FLEXTAG1, FLEXTAG2, FLEXTAG3, and HaloTag for PLIM-based super-resolution imaging. **b,** Top: Representative three-color live-cell SIM images of cells stably expressing TOM20-FLEXTAG1, MAP7-FLEXTAG2, and Sec61β-FLEXTAG3. Bottom: Magnified view of the boxed region highlighting the close spatial interactions among mitochondria, microtubules, and the ER. Scale

bars: 10 μm. **c,** Verification of orthogonality of FLEXTAGs. For each FLEXTAG, pixels were manually selected from corresponding organelles, and fluorescence intensities of the green (470 nm excitation), red (555 nm excitation), and far-red (640 nm excitation) channels were quantified. Boxplots show the mean and boundaries (first and third quartiles); whiskers denote SD. p-values calculated with two-sided unpaired Student's t-test. **d,** Representative fixed-cell SIM images of cells overexpressing TOM20-mEGFP-FLEXTAG1/FLEXTAG2/FLEXTAG3, labeled with 100 nM ET-JQ1-TMR, TMP-TMR, or SLF'-TMR. Scale bars: 10 μm. **e,** Representative two-color fixed-cell STED images with magnified views showing the potential spatial interactions between actin stress fibers and mitochondria. Left: Cells overexpressing TOM20-mEGFP-FLEXTAG1 and Lifeact-mEGFP-FLEXTAG2, labeled with 200 nM ET-JQ1-JF635 and 100 nM TMP-AF594; Right: Cells overexpressing TOM20-mEGFP-FLEXTAG2 and Lifeact-mEGFP-FLEXTAG3, labeled with 200 nM TMP-JF635 and 100 nM SLF'-AF594. Scale bars: 10 μm for full view, 5 μm for boxed region 1 (yellow), and 1 μm for boxed region 2 (blue). **f,** Schematic illustrating the anti-fading mechanism of self-renewable FLEXTAGs during prolonged imaging. Fluorescence intensity of non-renewable covalent protein tags progressively decreases over time due to the irreversible photobleaching of fluorophores (fading). In contrast, self-renewable protein tags continuously replace photobleached fluorophores with intact ones, thereby maintaining stable fluorescence intensity (anti-fading). **g,** Quantification of fluorescence intensity of FLEXTAG1/FLEXTAG2/FLEXTAG3/FKBP^{F36V}, and HaloTag over 30-frame live-cell SIM imaging, labeled with 100 nM ET-JQ1-MaP555/TMP-MaP555/SLF'-MaP555/SLF'-MaP555/HTL-MaP555. Three cells were imaged independently for each protein tag. Each frame was acquired at 1-minute intervals, and fluorescence intensities were normalized to the first frame. Data are presented as mean ± SEM. **h,** Representative time-lapse SIM images of a single live cell overexpressing TOM20-mEGFP-FLEXTAG1, FLEXTAG2, FLEXTAG3, FKBP^{F36V} or HaloTag, labeled with 100 nM MaP555 conjugated ligand. Images are shown at frames 1, 10, 20, and 30. Scale bars: 10 μm.

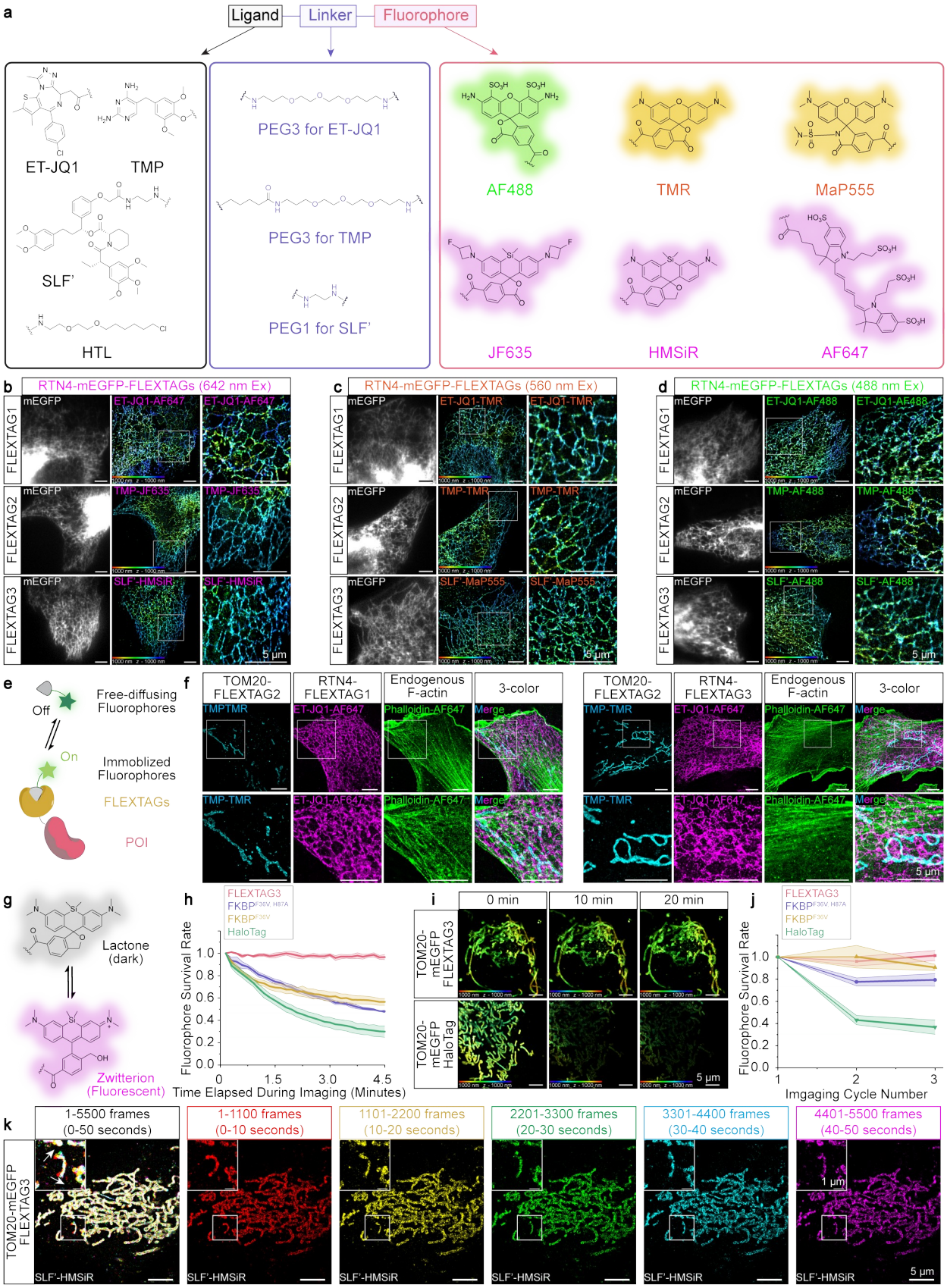
a
Ligand
Linker
Fluorophore
ET-JQ1
TMP
SLF'
HTL
PEG3 for ET-JQ1
PEG3 for TMP
PEG1 for SLF'
AF488
TMR
MaP555
JF635
HMSiR
AF647
b
RTN4-mEGFP-FLEXTAGs (642 nm Ex)
c
RTN4-mEGFP-FLEXTAGs (560 nm Ex)
d
RTN4-mEGFP-FLEXTAGs (488 nm Ex)
FLEXTAG1
FLEXTAG2
FLEXTAG3
mEGFP
ET-JQ1-AF647
TMP-JF635
SLF'-HMSiR
ET-JQ1-TMR
TMP-TMR
SLF'-MaP555
ET-JQ1-AF488
TMP-AF488
SLF'-AF488
5 µm
e
Off
On
Free-diffusing Fluorophores
Immobilized Fluorophores
FLEXTAGs
POI
f
TOM20-FLEXTAG2
RTN4-FLEXTAG1
Endogenous F-actin
3-color
RTN4-FLEXTAG3
TMPTMR
Phalloidin-AF647
Merge
g
Lactone (dark)
Zwitterion (Fluorescent)
h
FLEXTAG3
FKBP
HaloTag
Fluorophore Survival Rate
Time Elapsed During Imaging (Minutes)
i
0 min
10 min
20 min
TOM20-mEGFP FLEXTAG3
TOM20-mEGFP HaloTag
j
Imgaging Cycle Number
k
1-5500 frames (0-50 seconds)
1-1100 frames (0-10 seconds)
1101-2200 frames (10-20 seconds)
2201-3300 frames (20-30 seconds)
3301-4400 frames (30-40 seconds)
4401-5500 frames (40-50 seconds)
TOM20-mEGFP FLEXTAG3
SLF'-HMSiR
1 µm

Fig.7. FLEXTAG enables SMLM-based nanoscopic imaging with anti-fade performance. **a,** Chemical structures of ligand-linker-fluorophore conjugates targeting FLEXTAG1, FLEXTAG2, or FLEXTAG3 for SMLM-based super-resolution imaging. **b,** Far-red channel (642 nm excitation) single-color 3D-PAINT images of cells overexpressing RTN4-mEGFP-FLEXTAG1/FLEXTAG2/FLEXTAG3. FLEXTAGs were imaged with 1 nM ET-JQ1-AF647, 1 nM TMP-JF635, and 10 nM SLF'-HMSiR, respectively. Scale bars: 5 μm. **c,** Red channel (561 nm excitation) single-color 3D-PAINT images of cells overexpressing RTN4-mEGFP-FLEXTAG1/FLEXTAG2/FLEXTAG3. FLEXTAGs were imaged with 1 nM ET-JQ1-TMR, 1 nM TMP-TMR, and 1 nM SLF'-MaP555, respectively. Scale bars: 5 μm. **d,** Green channel (488 nm excitation) single-color 3D-PAINT images of cells overexpressing RTN4-mEGFP-FLEXTAG1/FLEXTAG2/FLEXTAG3. FLEXTAGs were labeled with 1 nM ET-JQ1-AF488, 1 nM TMP-AF488, and 1 nM SLF'-AF488, respectively. Scale bars: 5 μm. **e,** Schematic of FLEXTAG-PAINT. Fluorophore-conjugated FLEXTAG ligands transiently bind to self-renewable FLEXTAGs, producing stochastic localization events. Repeated binding and dissociation allow for the accumulation of single-molecule localizations over time, enabling reconstruction of a super-resolution (PAINT) image. **f,** Representative three-color PAINT images with magnified views showing the spatial interactions between actin stress fibers, mitochondria, and the ER. Left: Cells overexpressing TOM20-FLEXTAG2 and RTN4-FLEXTAG1, imaged with 1 nM TMP-TMR, 1 nM ET-JQ1-AF647, and 1 nM phalloidin-AF647 (For endogenous F-actin imaging). Right: Cells overexpressing TOM20-FLEXTAG2 and RTN4-FLEXTAG3, labeled with 1 nM TMP-TMR, 30 nM SLF'-HMSiR, and 1 nM phalloidin-AF647. Scale bars: 5 μm. **g,** Schematic of the HMSiR self-blinking mechanism for SMLM. HMSiR spontaneously switches between a dark lactone form and a fluorescent zwitterion form. **h,** Quantification of fluorophore survival rate in a single live-cell STORM movie (30,000 frames, 110 Hz, with total data acquisition time of 4.5 min). Three cells were imaged independently for each protein tag. Data are presented as mean ± SEM. **i,** Representative live-cell STORM images of cells overexpressing TOM20-mEGFP-FLEXTAG3 or TOM20-mEGFP-FKBP variants labeled with 30 nM SLF'-HMSiR, and cells overexpressing TOM20-mEGFP-HaloTag labeled with 30 nM HTL-JF630b (HMSiR has a ~9-fold higher duty cycle than JF630b so HMSiR is more prone to photobleaching[46])from three imaging cycles. Each cycle contains 4.5 min data acquisition time (30,000 frames, 110 Hz) and 5.5 min dark time. Scale bars: 5 μm. **j,** Quantification of fluorophore survival rates over three STORM imaging cycles. Data are presented as mean ± SEM. **k,** Live-cell STORM images of TOM20-mEGFP-FLEXTAG3 in the same field of view over 0–50 seconds (5,500 frames at 110 Hz). The boxed region with a magnified view highlights the gradual transition of mitochondria from a curved to a straight morphology over successive 10-second intervals (1,100 frames each). Scale bars: 5 μm (full view), 1 μm (boxed region).